Tumor-infiltrating nerves functionally alter brain circuits and modulate behavior in a mouse model of head-and-neck cancer

Jeffrey Barr [1†], Austin Walz [1†], Anthony C. Restaino[1,3], Moran Amit[4], Sarah M. Barclay[1], Elisabeth G. Vichaya[2], William C. Spanos[1,3], Robert Dantzer[4], Sebastien Talbot[5], Paola D. Vermeer[1,3,*]

[1]Sanford Research, Cancer Biology and Immunotherapies Group, Sioux Falls, South Dakota, USA.

[2]Baylor University, Department of Psychology and Neuroscience, Waco, TX, USA.

[3]University of South Dakota, Sanford School of Medicine, Vermillion, SD, USA.

[4]University of Texas, MD Anderson Cancer Center, Houston, TX, USA.

[5]Queen's University, Department of Biomedical and Molecular Sciences, Kingston, Ontario, Canada.

[†] equal first authors

*Corresponding author Email: Paola.Vermeer@sanfordhealth.org

Conflict of interest: RD is a consultant for GoodCap, Toronto; the consultancy is not related to the present work.

Abstract: Cancer patients often experience changes in mental health, prompting an exploration into whether nerves infiltrating tumors contribute to these alterations by impacting brain functions. Using a male mouse model for head and neck cancer, we utilized neuronal tracing techniques and show that tumor-infiltrating nerves indeed connect to distinct brain areas via the ipsilateral trigeminal ganglion. The activation of this neuronal circuitry led to behavioral alterations represented by decreased nest-building, increased latency to eat a cookie, and reduced wheel running. Tumor-infiltrating nociceptor neurons exhibited heightened activity, as indicated by increased calcium mobilization. Correspondingly, the specific brain regions receiving these neural projections showed elevated cFos and delta FosB expression in tumor-bearing mice, alongside markedly intensified calcium responses compared to non-tumor-bearing counterparts.

The genetic elimination of nociceptor neurons in tumor-bearing mice led to decreased brain Fos expression and mitigated the behavioral alterations induced by the presence of the tumor. While analgesic treatment successfully restored behaviors involving oral movements to normalcy in tumor-bearing mice, it did not have a similar therapeutic effect on voluntary wheel running. This discrepancy points towards an intricate relationship, where pain is not the exclusive driver of such behavioral shifts. Unraveling the interaction between the tumor, infiltrating nerves, and the brain is pivotal to developing targeted interventions to alleviate the mental health burdens associated with cancer.

Significance Statement: Head and neck cancers are infiltrated by sensory nerves which connect to a pre-existing circuit that includes areas in the brain. Neurons within this circuit are altered and mediate modifications in behavior.

Introduction:

The prevalence of mental health disorders (e.g., depression, anxiety, suicide) in cancer patients is significantly greater than in the general population [1-3]. For those patients with no prior psychiatric history, a cancer diagnosis increases the risk of mental health decline [4]. The presence of cancer introduces many stressors (physical, financial, relational) into the lives of patients, thus a negative impact on mental health may not be surprising. However, these changes persist even in long-term cancer survivors. For instance, decade-long cancer survivors maintain an increased incidence of depression (approximately 12%, depending on the cancer type) as compared to the population at large (3-5%) [5-7]. While the intensity and prevalence of psychological symptoms in cancer patients fluctuate before, during, and after treatment for a given type of cancer, and between cancer types, it remains higher than in the general population [8-10]. Whether the association of cancer with impaired mental health is directly mediated by the disease, its treatment or both remains unclear, yet it suggests that the development of a tumor may alter brain functions.

We have demonstrated the presence of TRPV1-expressing nociceptor neurons in head and neck squamous cell carcinomas (HNSCC) [11], melanoma, cervical [12], and ovarian cancers [13]. Nerve recruitment to the tumor bed is an active process that involves the release of soluble factors, including neurotrophins [14-16] and neuropeptides [17]. Tumor-released small extracellular vesicles (sEVs) also recruit loco-regional nerves to the tumor bed [11,18]. While these and other studies establish that solid peripheral tumors engage with the peripheral nervous system [11,13,19-23], it raises the possibility of a direct neuronal connection from the tumor to the brain.

A recent study used pseudorabies virus and mapped a connection from tumor-infiltrating nerves in an orthotopic model of murine lung cancer to areas in the brain [24]. We expand these findings and demonstrate that HNSCC-associated nerves are transcriptionally and functionally altered and project to discrete regions in the brain. The brain neurons connected to the tumor harbor increased activity, which is associated with behavioral alterations in tumor-bearing animals. Consistent with this, newly diagnosed HNSCC patients suffer high rates of depression and anxiety and lower quality of life [25]. As most cancer patients face cancer-related pain [26-28], we tested whether treating pain could restore normal behavior. While pain treatment restored normal function at the tumor site, such as nesting behavior, it only partially restored normal voluntary running wheel behavior. Our findings suggest that, in addition to pain, tumor-infiltrating nerves communicate signals to the brain that lead to cancer-associated changes in behavior.

Results

Tumor innervation begins early in disease. MOC2-7 cells are HNSCC cancer cells derived from a CXCR3 null mouse under a C57BL/6 background [29]. Their implantation in male mice results in dense innervation of tumors with nociceptor nerves[38,39]. To define the timing of tumor innervation, wildtype male mice were orthotopically implanted (oral cavity) with MOC2-7 cells, and tumors were collected on days 4-, 10-, and 20- post-implantation. Western blot analysis of whole tumor lysate indicated expression of Tau, a neuronal marker [40], as early as day four post-tumor implantation, which increased over time (**Fig. 1A**; full westerns in **Supplemental Fig. 1A-B**; densitometric quantification of westerns, **Supplemental Fig. 1E**). A similar increase in the neuronal marker doublecortin (DCX) was noted (**Fig. 1B**; full western **Supplemental Fig. 1C-D**; densitometric quantification of westerns, **Supplemental Fig. 1F**). While DCX is well-known for

its expression in immature neurons, it is also expressed in adult peripheral neurons, including dorsal root ganglia [41], and in non-neuronal tissues[42]. The DCX signal did not originate from the tumors, as MOC2-7 cell lysate was negative for this protein (**Fig. 1B**, Full western **Supplemental Fig 1C**). Consistent with this, immunohistochemical staining of these tumors with the neuronal marker β-III tubulin (β3T), demonstrated the increasing presence of nerves beginning on day four post-tumor implantation (**Fig. 1C-E**).

Tumor-infiltrating nerves map to the ipsilateral trigeminal ganglion and into the CNS. To map the origin of tumor-infiltrating nerves and define the circuits they converge upon, mice with palpable oral MOC2-7 tumors (approximately day 15 post-tumor implantation) were intra-tumorally injected with wheat germ agglutinin, WGA, a neural tracer conjugated to a fluorophore (n= 10 mice). WGA is a lectin molecule that specifically binds to sialic acid residues present ubiquitously on neuronal membranes. It has been utilized extensively to map neuronal circuits centrally and in the periphery [43,44] and is a known transganglionic and transynaptic neuronal tracer [45-47] making it ideal for mapping neural circuits [48-52]. Following tracer injection, tumor growth was permitted for an additional 3-7 days to allow time for tracer labeling to occur. Animals were then euthanized, and tumors, trigeminal (TGM) ganglia, and brains were harvested and analyzed by microscopy. Microscopic examination of tumors revealed nerves with robust WGA signals (**Fig 1F**) as well as the V3 branch of the ipsilateral, but not the contralateral, TGM ganglion (**Fig 1G,H**). Consistent with the restricted labeling of tumor-infiltrating nerves, the tracer did not diffuse outside the tumor mass (**Fig. 1I**).

Examination of brains from MOC2-7 tumor-bearing animals revealed tracer^{+} neurons in specific regions [including spinal nucleus of the trigeminal (SpVc), parabrachial nucleus (PBN), and central amygdala (CeA)] (**Fig 1J**). Sections of brain from these regions show the presence of

tracer-positive neurons (**Fig 1K**). Tracer injections of equivalent volume and concentration into the oral cavities of control non-tumor-bearing animals did not label the TGM ganglia nor areas in the brain (data not shown). A larger volume (10µl) of tracer injected into non-tumor bearing mice resulted in tracer labeling of ipsilateral TGM neurons and brain (**Fig. 1L**). These control studies indicate that the nerve density and distribution present in the tumor bed are higher than in control mice, with the consequence that a small volume (2 µl instead of 10 µl) of tracer is sufficient to result in nerve labeling. The mapped circuit encompasses pre-existing connections to brain areas that regulate pain and affect [53-56]. These data indicate that the nerve infiltration into the tumor extends this circuit.

Tumor-infiltrating neurons are transcriptionally modified. The observation of nerves infiltrating the tumor mass prompted us to ask whether they undergo alterations by their mere presence within this "foreign" environment. Consistent with this, we previously found that melanoma-infiltrating neurons have a unique transcriptome [57]. To test whether this is also the case in HNSCC, we orthotopically implanted MOC2-7 cells into the oral cavity of male wildtype mice. After 14 days, TGM neurons were harvested and analyzed by qPCR using a commercial array for neural transmission and membrane trafficking genes. Compared to control TGM (non-tumoral) neurons, ipsilateral TGM neurons from tumor-bearing animals harbored increased expression (<4-fold) in genes involved in neuronal signaling/receptors (*Gabrg1*, *Gabra4*, *Grin2c*, *Grm3*) and synaptic transmission (*Gria2*) (**Fig. 2A; Supplemental Table 1**) [58]. Of note, we purposefully used whole trigeminal ganglia rather than FACS-sorted tracer-positive dissociated neurons to avoid artificially imposing injury and altering the transcriptome of these cells [59,60].

Tumor-infiltrating neurons are functionally changed. Given this transcriptomic alteration, we tested whether tumor-infiltrating neurons exhibit functional alterations. Thus, MOC2-7 tumor-bearing mice were intra-tumorally injected with the fluorophore-conjugated WGA tracer. Five days later, tracer^{+} TGM ganglia were cultured, and responsiveness to noxious stimuli was analyzed by calcium microscopy. Neuronal Ca^{+2} responses to capsaicin (300 nM), which binds and activates TRPV1 channels, were measured by Fluo-4AM fluorescence microscopy. We found that tracer^{+} tumor-infiltrating ipsilateral TGM neurons show increased responsiveness to capsaicin compared to tracer negative contralateral neurons (amplitude, **Fig. 2B-D;** the area under the curve**, Fig. 2E**). Similar to contralateral TGM neurons, non-tumor-bearing TGM neurons elicited a normal response to capsaicin (**Fig. 2F**).

This heightened sensitivity could reflect increased TRPV1 expression and/or its phosphorylation. We tested whether this was the case using western blotting and discovered an overexpression of the sigma 1 receptor (σ1R) and increased TRPV1 phosphorylation in the TGM ganglia from tumor-bearing animals (**Fig. 2G-I,** full westerns **Supplemental Fig 2A-C**). Of note, the σ1R is an endoplasmic reticulum chaperone protein that directly interacts with TRPV1 and regulates its membrane expression, [61] while protein kinase C phosphorylation of serine 502 and 800 of TRPV1 reduces the receptor's activation threshold [62-65]. Taken together, our data indicate that HNSCC-infiltrating nerves have a unique transcriptome and a heightened sensitivity to noxious stimuli characterized by an increased TRPV1 expression and phosphorylation consistent with TRPV1 sensitization secondary to oral cancer [66].

Tumor-brain circuit neurons harbor elevated activity. The transcriptional and functional changes evident in tracer^{+} tumor-infiltrating neurons could result in alterations in central target neurons. To assess this, brain sections from MOC2-7 tumor-bearing and non-tumor-bearing

animals were immunofluorescently stained for cFos and ΔFosB, two markers of neuronal activity with different courses of expression [67-69]. ΔFosB expression was increased in several brain regions of tumor-bearing animals, while cFos expression was also increased in the PBN (**Fig. 3A-F**). Predominant differences in the long-lived ΔFosB were expected [70], as those with the short-lived cFos changes are more challenging to capture using single time point assessment.

Next, we assessed the neuronal activity of tumor-bearing animal brains using stereotaxically injected AAV1-Syn-GCaMP6f, a viral vector encoding a neuron-specific synapsin-driven calcium sensor [71], into the PBN. Two weeks after intra-cranial injection of the virus, mice were orally implanted with MOC2-7 cells. Approximately 18 days post-tumor inoculation, the animals were euthanized, and the neuronal calcium activity was recorded in *ex vivo* brain slices using a mini scope (**Suppl Fig. 3A,B)**. While baseline fluorescence was similar between tumor-bearing and control animals, that recorded upon stimulation (KCl; 30 mM) was significantly higher in neurons of tumor-bearing animals (**Fig. 3G-J; Supplemental Fig 3A,B**). These functional and Fos staining data indicate that central neurons within the tumor-brain circuit are functionally altered compared to their healthy brain counterparts.

Ablation of tumor-infiltrating neurons attenuates cancer-induced brain alterations. Cancer patients, and even more notably, survivors, experienced poor mental health [1,72-74]. The neural connection between tumor and brain, together with our finding that TRPV1-expressing nociceptor neurons within this circuit become functionally altered, might contribute to these changes. To test whether this is the case, we genetically engineered mice with ablated nociceptor neurons ($TRPV1^{cre}$::$DTA^{fl/wt}$). $TRPV1^{cre}$::$DTA^{fl/wt}$ animals lack TRPV1-expressing cells (including neurons) as well as many other nociceptive neurons. These nociceptor neuron ablated mice have been previously characterized and lack the expected sensitivity to temperature as well

as itch and pain reactions to chemical mediators such as capsaicin [75]. cFos and ΔFosB immunostaining of brains from nociceptor ablated and control (C57BL/6) mice show no significant differences (**Supplemental Fig 3C-E**) indicating that, in the absence of a malignancy, the neurons in these regions are not differentially activated. First, we confirmed the absence of TRPV1^{+} neurons in the TGM of these ablated animals (**Fig. 4A**). We then analyzed cFos and ΔFosB expression in the brain of MOC2-7-bearing nociceptor intact and ablated mice. While Fos expression was similar between non-tumor bearing mice of the two genotypes (**Supplemental Fig. 3C-E**), the absence of nociceptor neurons decreases cFos and ΔFosB in the PBN, and ΔFosB in the SpVc (**Fig. 4B, C**). Other tested regions were not impacted (**Fig. 4D**). These data suggest that the tumor-brain communication was disrupted in the absence of nociceptor neurons.

Alleviation of pain does not always restore behavior. To evaluate the effects of this disruption on cancer-induced behavioral changes, we assessed the animals' general well-being through nesting behavior [32] and anhedonia using the cookie test [76,77], as well as body weight and the speed of food disappearance as a surrogate for oral pain. Nociceptor neuron ablated mice showed increased nesting performance (**Fig. 4E**) and decreased anhedonia (**Fig. 4F**) compared to intact mice. This was accompanied by smaller tumor growth (**Fig. 4G**) and increased survival (**Fig. 4H**). While both groups showed similar body weight loss (**Fig. 4I**), nociceptor ablated animals show a transient (Wk 1, 4, 5) decrease in food disappearance (**Fig. 4J**). Significant effects for all statistical analyses in Figure 4 are presented in Supplementary Table 2.

The developmental ablation of TRPV1 neurons can lead to unintended effects on tumor innervation and behavior. Thus, we chemoablated TRVP1 neurons in 4-week-old juvenile C57BL/6 mice using resiniferatoxin (RTX) [39,40]. We examined nesting behavior in RTX and vehicle-treated C57BL/6 male mice orthotopically implanted with MOC2-7 cells. An additional

control group consisted of age-matched C57BL/6 mice without tumors. Although all groups displayed similar nesting scores initially, the scores in vehicle-treated mice declined significantly faster compared to RTX-treated mice (**Fig 5A**). Body weight decreased in all tumor-bearing mice, but the extent of weight loss was similar between vehicle and RTX-treated mice (**Fig 5B**). Similar to the developmental ablation of TRPV1 neurons, their chemoablation post-development results in a similar decrease in tumor growth compared to controls (**Fig 5C**).Since HNSCC tumors cause oral pain and both nesting and the cookie test require the use of the mouth, we also evaluated the effect of nociceptor ablation on voluntary wheel running to gain additional insights into cancer-associated fatigue, a surrogate for depressive-like behaviors in tumor-bearing mice [78-82]. To assess the potential influence of cancer-associated pain, 1-week post tumor inoculation, groups of mice were treated with carprofen (a non-steroidal anti-inflammatory), extended-release buprenorphine (opioid), or vehicle. We found that wheel running decreased as tumors progressed, an effect partially alleviated by carprofen and buprenorphine (**Fig 6A,B**). The nesting behavior (**Fig 6C**), body weight (**Fig 6D**), and food disappearance (**Fig 6E**) were also alleviated by the painkillers. Neither carprofen nor buprenorphine impacted MOC2-7 tumor growth compared to vehicle-treated animals (**Fig 6F**), but buprenorphine increased tumor growth compared to carprofen-treated mice (significant effects for all statistical analyses in Figure 5 are presented in Supplementary Table 3). These findings suggest that choosing pain management drugs in the context of cancer can potentially influence tumor growth adversely. Furthermore, the data reveals that behaviors associated with the tumor site are adversely affected by cancer-associated pain. However, merely alleviating pain does not fully restore all behaviors, as evidenced by persistent issues in activities like wheel running.

Discussion

We have previously demonstrated that head and neck squamous cell carcinoma is associated with innervation by sensory neurons and that substance P, one of the principal neuropeptides these fibers release, drives malignant cell proliferation and migration [38]. Significantly, patients suffering from HNSCC often experience depressive disorders, which are poorly managed clinically [83-85]. Here, we now found that nociceptor neurons infiltrating HNSCC connect to a pre-existing brain-projecting circuit [86,87] that includes the trigeminal ganglia, the spinal nucleus of the trigeminal (SpVc), as well as the parabrachial nucleus (PBN), and central amygdala (CeA). This connection occurs independently of pain, and this cancer-brain circuit drives behavioral alterations in tumor-bearing mice. While the elimination of TRPV1-expressing nociceptor neurons reduces tumor growth and enhances survival rates, it also highlights a potential therapeutic target for mitigating depressive behaviors in cancer patients. This underscores the complex interplay between sensory neurons, cancer progression, and mental health, uncovering a two-pronged approach to improving HNSCC patients' physical and psychological health.

In melanoma [57] and HNSCC, we demonstrated significant transcriptional alterations within tumor-infiltrating nerves. Several mechanisms can account for these changes. For instance, TRPV1 stimulation is sufficient to trigger the activation of the AP-1 transcription factor within neurons [88]. Such TRPV1 activation could occur in response to low pH [89] or hypoxia [90-92], which are both prevalent within the tumor microenvironment. Alternatively, we previously demonstrated that tumor-released sEVs, which transport microRNAs (miRNAs), induced sprouting of loco-regional nerves to the tumor bed [11,93]. These sEV-transported miRNAs could

also modulate various neuronal transcription factors and, in turn, drive the transcriptomic changes we observed in these neurons.

Our data indicate that these peripheral neuronal changes also influence the functioning of the brain areas to which they connect. Although we did not make the complete cartography of all brain regions utilized by tumor-infiltrating nerves, we identified a few critical nuclei. Subsequent work will use emerging circuit mapping techniques for whole brain profiling [94]. Nevertheless, our tracing in tumor-bearing nociceptor neuron ablated, and intact animals was sufficient to functionally implicate TRPV1-expressing neurons in this communication.

Trigeminal ganglia neurons are composed of ~80% of $Na_V1.8^+$ nociceptor neurons, with one-half being peptidergic ($TRPV1^+$, $TRPA1^+$) neurons [95,96,75]. In the $TRPV1^{cre}$::$DTA^{fl/wt}$ mouse, these peptidergic neurons are eliminated, leaving intact ~50% of pain-sensing neurons. The remaining presence of these non-peptidergic, largely $MrgD^+$, neurons might explain why nesting behavior in $TRPV1^{cre}$::$DTA^{fl/wt}$ tumor-bearing animals is only partially restored.

Inflammation contributes to pain in cancer [97]. Consistent with this, treatment of tumor-bearing mice with analgesic drugs (carprofen, buprenorphine) resulted in complete restoration of nest building and performance in the cookie test. These data show that the constraint imposed by the tumor on behavioral activities that require the use of the oral cavity is mainly due to pain and not to the physical interference of the tumor mass with the pattern of oral activities that need to take place for mice to perform the corresponding behavior.

Cancer pain often interferes with activities that don't involve oral movements, a phenomenon evident in the impaired voluntary wheel running observed in tumor-bearing mice. Although analgesic drugs can partially mitigate this deficit, they fail to restore this behavior fully, despite their efficacy in completely restoring oral activity behaviors like nesting and the cookie test. This suggests that factors beyond pain contribute to the observed behavioral changes. These alterations could be attributed to depression [98] or represent a competition between the energy demands of the HNSCC malignant cells and the host's skeletal muscles [99-101].

Our current findings suggest that interrupting tumor-to-brain communication can mitigate the mental health decline often associated with cancer. Yet, a higher prevalence of depression persists among long-term cancer survivors compared to individuals without a cancer history. Having received treatment and showing no evidence of disease, these survivors continue to battle mental health issues [6,7]. This phenomenon prompts a critical question - why does this discrepancy exist? It is conceivable that these patients, through treatments like surgery, radiation, or chemotherapy, have disrupted the tumor-brain connection and have sustained this disconnection over the years. However, unlike animal models, their mental health decline is not reversed. Several speculations, grounded in known factors, can be considered.

The human experience with cancer is distinct from that of mouse models; individuals can live with malignant growths for extended periods, often unaware of their existence due to asymptomatic or nonspecific symptoms. During this undiagnosed period, the tumor-brain circuit might induce irreversible changes in central neurons through activity-dependent transcriptional

modifications [102,103]. These alterations, anchored in neuronal plasticity, adaptation, and behavior, may become permanent even after the cancer is diagnosed and treated.

Moving forward, to reverse these entrenched brain changes, understanding the specific transcriptional alterations incurred by central neurons is vital. Unraveling this complexity could pave the way for therapies that reverse the neuronal activity impacts, fostering improved mental health. Although in its early stages, our insight into the role of nerves in cancer is growing, and highlighting neuronal targets for pharmacological interventions.

Our study is not exempt from limitations. First, our exploration of the tumor-to-brain pathway was confined to mice with HNSCC and utilized a single cancer cell line. Hence, the universality of our conclusions warrants verification through additional HNSCC cell lines and diverse cancer models. Furthermore, the exclusive focus on HNSCC, particularly considering the nerve-rich oral region, raises questions about the pathway's establishment and behavioral impact in other contexts. Our behavioral assessment was not exhaustive; a comprehensive analysis of nerve-dependent and independent behaviors remains forthcoming. Behaviors could also be influenced by elements like soluble factors or the energy competition between the tumor and behavioral activities. Our studies have also solely involved male mice, presenting a clear gap in understanding the potential sex differences in the development of the tumor-to-brain communication pathway and its subsequent influence on behavior. The inclusion of female subjects in future research is essential to provide a comprehensive insight into these processes.

Second, our nerve tracing methodology, where we injected 2 µl of WGA into the tumor bed, is designed to label only the tumor-infiltrating nerves and their connections. However, this approach fails to label *all* tumor-infiltrating nerves, predominantly those not close to the WGA-injected region and nerves that are in contact with or influenced by the tumor but are not directly infiltrating it. This limitation is a calculated one, reflecting a technical trade-off. We aimed to ensure the specificity of capturing only tumor-infiltrating nerves, which meant sacrificing the comprehensiveness of labeling all nerves associated with the tumor. This constraint extends to our calcium imaging studies and brain tracing. Although we can confidently assert that all labeled neurons are indeed tumor-infiltrating or connected, we cannot conclusively state that all tracer-negative ipsilateral nerves are unconnected to the tumor-brain circuit.

Even with these constraints, our findings are important. We have demonstrated that tumor-infiltrating nerves are integrated into a pre-established neuronal circuit. This circuit extends from the tumor bed to the TGM ganglion, connects to the SpVc, and projects into the brain, influencing behavior in both pain-dependent and independent ways. This revelation paves the way for in-depth exploration into the mechanistic underpinnings of cancer-associated alterations in well-being and mental health, shedding light on potential therapeutic interventions to alleviate these profound effects.

MATERIALS AND METHODS

Study approval. All animal studies were performed with approval from the Institutional Animal Care and Use Committee at Sanford Research and were within institutional guidelines and

complied with all relevant ethical regulations. Sanford Research has an Animal Welfare Assurance on file with the Office of Laboratory Animal Welfare (assurance number: A-4568-01) and is accredited by AAALAC, Intl. Sanford Health is also a licensed research facility under the authority of the United States Department of Agriculture (USDA) with USDA certificate number 46-R-011.

Inclusion & Ethics Statement. All studies utilizing animals were performed with approval from the appropriate ethical bodies to ensure sufficient protection was in place. This study was a collaborative, multi-disciplinary, multi-institutional effort with contributions from researchers in academic positions.

Cell lines. MOC2-7 cells (RRID:CVCL_ZD34) [29] (previously known as MOC7) [30] were a kind gift from Dr. Ravindra Uppaluri (Dana-Farber Cancer Institute, Boston, MA). They were maintained in DMEM with 10% fetal calf serum and cultured at 37°C and 5% CO_2; with culture medium refreshed every three days. These cells can be obtained through Kerafest (www.kerafest.com).

Animal studies. All animal experiments were performed in the Sanford Research Animal Resource Center which is a specific pathogen free facility. All mice were maintained in IVC Tecniplast Green line Seal Safe Plus cages which were opened only under aseptic conditions in an animal transfer station. All cages were changed every other week using aseptic technique. All cages had individual HEPA filtered air. Animal rooms were maintained at 75°F, 30-70% humidity, with a minimum of 15 air changes per hour, and a 14:10 light/dark cycle. Corncob

bedding, which was autoclaved prior to use, was maintained in all cages. Irradiated, sterile food (Envigo) and acidified water (pH 2.8-3.0) were available *ad libitum*. There was a maximum of 5 mice/cage. All animals were observed daily for abnormal behavior, signs of illness or distress, the availability of food and water and proper husbandry. Animals injected with murine tumor cells were 10-week-old C57BL/6 or TRPV1^{cre}::DTA$^{fl/wt}$ mice (The Jackson Laboratory) weighing approximately 24 gm. Investigators were blinded to the groups when assessing animals (e.g., measuring tumors). Animals were numbered by ear punch and cage number.

Nociceptor neuron ablated TRPV1^{cre}::DTA$^{fl/wt}$ animals were generated by crossing ROSA26-DTA (diphtheria toxin A, B6.129P2-*Gt(ROSA)26Sor* $^{tm1(DTA)Lky}$/J) and TRPV1-Cre (B6.129-*Trpv1*$^{tm1(cre)Bbm}$ /J) [31] mice; the progeny (TRPV1^{cre}::DTA$^{fl/wt}$) express DTA (diphtheria toxin fragment A) under control of the TRPV1 promoter, thereby genetically ablating all TRPV1 expressing cells (including TRPV1-expressing neurons) throughout development. Absence of TRPV1-expressing sensory neurons was validated by IHC staining of TGM ganglia for TRPV1. Chemoablation of TRPV1-expressing neurons post-development was accomplished with resiniferatoxin (RTX), a naturally occurring potent TRPV1 agonist. RTX treatment results in the specific ablation of TRPV1 neurons (post-development), while sparing other TRPV1 expressing (non-neuronal) cells. RTX treatment in mice consisted of three injections of RTX given 24 hours apart. The injections are given in the flank and were: 30ug/kg on day 1, 70ug/kg on day 2 and 100ug/kg on day 3. Just prior to the first RTX injection, mice are treated with 0.1 mg/kg of buprenorphine, given intraperitoneally, as the first injection causes pain. Subsequent injections do not require buprenorphine. It takes 4 weeks for TRPV1 nerve ablation to occur. Control mice

received injections with vehicle solution (DMSO with Tween80 in PBS). The tail flick test was used to confirm nerve ablation.

Tail flick test. Prior to testing, mice are acclimated to the room for 30 minutes. A water bath is pre-warmed to 52□C and a thermometer is used to constantly monitor the temperature of the water. The mice are picked up using a fresh paper towel so that only their tail is outside the paper towel. Once the mouse is relaxed in the tester's hand, the mouse's tail is lowered into the water so that a quarter of the tail is submerged. The time for the tail to be flicked out of the water is recorded. If no response has occurred by 20 seconds, the mouse's tail is removed from the water to prevent tissue damage. A response time latency greater than 10 seconds signifies denervation.

Tumor implantation. Ketamine (87.5 mg/kg)/xylazine (10 mg/kg) were used to anesthetize mice prior to oral cavity tumor implantation. Tumors were initiated as follows: using a 25-gauge needle, cells (5 x 10^4 cells in a total of 50 μl) were implanted orthotopically in the oral cavity of male C57BL/6 mice. Specifically, the needle was placed proximal to the crease of the mouse cheek, inserted at approximately a 45° angle, bevel deep, and tumor cells injected into this location of the cheek pouch. Mice were allowed to recover from anesthesia on a heating blanket and returned to their home cage. Control (non-tumor) mice were treated the same way only their injection contained media alone (no cells). Tumor growth was monitored weekly by caliper measurements of isoflurane anesthetized animals and tumor volume calculated was using the formula: ½ (length*(width^2)).

Drug treatments. Carprofen (Pivetal) was provided in the drinking water (10mg/kg which is equivalent to 0.067 mg/ml) which was refreshed every 7 days. Buprenorphine-ER (Fidelis

Animal Health), a 72-hour extended-release formulation, was given by subcutaneous injection (3.25 mg/kg) every 72 hours. Vehicle-treated animals were treated with subcutaneous injection of saline. Drug treatments commenced on day 7 post-tumor implantation in all groups. Given that buprenorphine treatment requires a subcutaneous injection every 3 days, mice in the other groups (vehicle and carprofen) received a subcutaneous injection of saline at the same volume (60 µl) as the buprenorphine-treated animals. In this way, all animal stress from handling and injection was the same.

Nest building. Nest building is an innate behavior performed in rodents of both sexes and is a general indication of well-being [32]; it also measures the motivation to perform a goal-directed task. To assess nesting behavior, individually housed mice were given a nesting square (Ancare) overnight. The following morning, nests were scored by two independent scorers who were blinded to the conditions [33,34]. The scoring system is 0-4 and based on the percentage of the nestlet that is shredded and the height of the nest. Two baseline measurements were conducted prior to tumor implantation followed by weekly testing. Exclusion criteria of an average baseline score of 3 or greater was used to ensure all mice were good nest builders at baseline (n=3 C57BL/6 mice and n=7 $TRPV1^{cre}$::$DTA^{fl/wt}$ mice were excluded for this reason).

Cookie test: The cookie test is a variation of the sucrose preference test, a test of anhedonia (the inability to experience enjoyment or interest in previously rewarding activities). These test the animal's endogenous inclination for sweet tastes and the notion that it derives pleasure from consuming sweets. One hour prior to testing, the mice were fasted and acclimated to the brightly lit testing room. Following the acclimation period, mice were given a piece of cookie

(approximately 1.5 gm). The time it took the mouse to bite the cookie from its placement in the cage was measured to determine time-to-interact. Each mouse was acclimated to the cookie every other day for 2 weeks prior to tumor implantation with a baseline measurement followed by weekly testing. Mice were individually housed. One mouse from the C57BL/6 group was excluded due to incomplete data (mouse died before completion of the study).

Voluntary wheel running: Prior to tumor implantation, mice were singly housed with a running wheel maintained in the home cage continuously. The only time that the wheel was removed was when mice were undergoing nesting. The mice were acclimated to the wheel for 2 weeks prior to tumor implantation. This acclimatization period provided the time to stabilize their running performance. Running wheels were maintained in the home cage for the duration of the study. As mice are most active during the dark phase, nighttime running (8pm to 8am) was assessed. Running data were collected in 1-minute bins continuously throughout the duration of the experiment.

Food disappearance. Animals were provided 100 g of solid food per cage each week. At the end of each week, the remaining food was weighed, and this value was used to calculate the amount of food that disappeared in that week per cage. For all behavioral experiments, mice were singly housed.

Neural tracing of orthotopic HNSCC tumors. When oral tumors reached approximately 5 x 5 mm in size, neural tracer was injected into the tumor as described below. Ketamine (87.5 mg/kg)/xylazine (10 mg/kg) were used to anesthetize the mice. A 10 µL Hamilton syringe with

30-G needle was loaded with 1% Wheat Germ Agglutinin (WGA) conjugated to either AlexaFluor 594 (Invitrogen) or CF568 (Biotium) in PBS and 2µl was slowly injected intra-tumorally with the bevel side up. The needle was inserted approximately midway through the tumor then pulled back slightly to reduce pressure and leakage of tracer following injection. The injection of tracer occurred slowly over the course of 10 minutes. After the tracer was injected, the needle was kept in place for 2 additional minutes before being slowly removed. Mice were placed on a heating pad until recovery from anesthesia. Five to seven days later, mice were deeply anesthetized and transcardially perfused with ice cold PBS followed by 4% paraformaldehyde and trigeminal ganglia (TGM) were carefully removed and placed in HBSS in a 24-well plate kept on ice. TGM harvesting was completed as follows: euthanized animals were subjected to a midline incision while in the prone position to expose the crown of the skull. The brainstem was separated from the spinal cord by a transverse cut and the top of the skull was removed, exposing the brainstem and TGM. All tissues (tumor, ganglia and brain) were fixed, sectioned, and imaged for WGA labeled nerve fibers and somas under confocal microscopy. WGA injection into control (non-tumor bearing animals) was performed the same way and injection was into the same oral region where tumors were implanted. Volumes of 2 or 10 µl of WGA were used.

Immunohistochemical (IHC) staining. Tissues were formalin fixed, paraffin-embedded and cut into 5 µm sections. The BenchMark® XT automated slide staining system (Ventana Medical Systems, Inc.) was used to optimize antibody dilutions and staining. The Ventana CC1 solution was used to perform the antigen retrieval step (basic pH tris base buffer). Tissues were incubated

in primary antibody for 1 hour. The Ventana iView DAB detection kit was used as the chromogen and the slides were counterstained with hematoxylin.

Antibody utilized for immunohistochemistry (IHC). Anti-β-III Tubulin (Abcam, Cat# ab78078, 1:250, RRID: AB 2256751), Anti-TRPV1 (Alomone Labs Cat# ACC-030, 1:400, RRID:AB_2313819).

Antibodies utilized for immunofluorescence (IF). cFos (Cell Signaling, Cat# 2250, 1:10,000, RRID: AB 2247211), ΔFosB (Abcam, Ab11959, 1:5,000, RRID:AB_298732). The following secondary antibodies were used: Alexa568 anti-rabbit (Thermo, Cat# A-11011, 1:500, RRID:AB_143157), Alexa488 anti-mouse (Thermo, Cat# A-11001, 1:500, RRID:AB_2534069).

Antibodies utilized for western blot. β-actin (Sigma Life Science, Cat#A2228, 1:1000, RRID: AB_476697), Tau (Abcam, Cat# ab75714, 1:500, RRID:AB_1310734), phosphorylated TRPV1 (Thermo Fisher Scientific, Cat# PA5-64860, 1:500, RRID:AB_2663797), Sigma-1R (ProteinTech, Cat# 15168-1-AP, 1:1,000, RRID:AB_2301712), Doublecortin (DCX) (Santa cruz, Cat# sc-271390, 1:1000, RRID:AB_10610966).

Brain immunostaining and analysis. Brains were post-fixed for twenty-four hours. Coronal or sagittal sections were cut at 40 µm using a vibratome. Sequential fluorescent immunolabeling was performed for cFos or ΔFosB on free-floating sections. All sections were blocked with 10% goat serum in 0.3% Tx-100. All antibodies were diluted in PBS containing 0.03% Triton X-100 and 2% normal goat serum. Sections were incubated in Fos antibody for 72 hours. Following

washes in 0.1M phosphate buffered saline, sections were incubated in secondary antibody for 3 hours. Following additional washes, sections were mounted onto glass slides, and cover slipped with cytoseal prior to imaging. The total numbers of cFos or ΔFosB-labeled nuclei were counted on 10 × 2D images acquired using a laser-scanning confocal microscope (Nikon A1R) and verified as positive if the signal filled the nucleus and stood out clearly compared to surrounding tissue [35]. Nuclei were counterstained with DAPI. Quantification of Fos-labeled cells was performed using digital thresholding of Fos-immunoreactive nuclei. The threshold for detection was set at a level where dark Fos-immunoreactive nuclei were counted, but nuclei with light labeling, similar to background staining, were not. For each animal, 3-4 sections were selected at 120 μm intervals. ImageJ cell counter (v. 1.52) was used to quantify Fos+ nuclei per region / section.

Analysis of transcriptional changes in tumor-infiltrating neurons. To assess transcriptional changes in tumor-infiltrating neurons we utilize a qPCR array (ScienCell, GeneQuery Neural Transmission and Membrane Trafficking, #MGK008). These qPCR-ready 96 well plates enable rapid profiling of 88 key genes important for neuronal functions (listed in Table S1). Mice bearing MOC2-7 oral tumors were injected with tracer (as described above); TGM ganglia were isolated on day 28 post-tumor implantation, their RNA harvested, converted into cDNA and then assayed with the array as per manufacturer's instructions (ScienCell, GeneQuery arrays). We utilized N=4 TGM/group from n=4 mice/group; n=4 plates/condition. Control RNA was isolated from TGM ganglia from age-matched non-tumor bearing mice (n=4 mice). Relative gene expression was calculated as per manufacturer's recommendations.

Western blot analysis of whole tumor lysate. Tumors were excised from euthanized mice, taking care to eliminate as much non-tumor tissue as possible. Tumors were then placed in approximately 500µl lysis buffer (50mM Tris HCl pH 7.4, 100mM NaCl, 100mM NaF, 10mM NaPPi, 2mM Na_3VO_4, 10% glycerol, HALT protease inhibitor cocktail) with 1% TX-100 and kept on ice for 10 minutes. The homogenate was sonicated 3x for 15 secs and then incubated on ice for 15 minutes. Samples were then centrifuged at 2000 g for 5 minutes at 4°C, supernatant was collected and further centrifuged at 12,000 g for 10 minutes at 4°C. Protein concentrations of the supernatants were determined by BCA protein assay.

Western blot analysis of ganglia lysate. Trigeminal ganglia were harvested as described above. Ganglia were lysed using a homogenizer in lysis buffer at 4°C. Homogenates were centrifuged at 10,000 g for 20 minutes and protein concentrations determined from the supernatant. Protein concentration was measured by BCA protein assay (Pierce, Cat#23225) and 40 ug of total protein were separated by SDS-PAGE, transferred to PDVF membranes which were then blocked for 30 minutes at room temperature (RT) in 5% milk in PBS. Membranes were incubated with primary antibody overnight at 4°C. Following 1xTBST washes, membranes were probed with an HRP-conjugated secondary antibody (1:10,000 dilution) for 1 hour at RT, washed and imaged on a Li-COR Odyssey FC imaging system. Densitometric quantification was used to assess changes in protein expression.

Western blot densitometry analysis. Raw images of western blots were analyzed using ImageJ. Briefly, images were opened and bands of interested were selected by gating with the rectangle selection tool. Densitometry was measured based on grey scale analysis of selected area.

Analysis was conducted on proteins of interest as well as the loading control band (β-actin). Relative expression of proteins of interest was determined as a fraction of β-actin densitometry.

Neuron culture. Trigeminal ganglia were harvested from MOC2-7 tumor-bearing or non-tumor animals and enzyme digested in papain, and then collagenase II/dispase at 37 □ for 15 min. After washing and trituration, cells were plated onto a thin layer of Matrigel® in glass bottom dishes and cultured with HamsF12 supplemented with 10% FBS. The cells were maintained in an incubator (5% CO_2, 37 °C) for 24 h before they were used for calcium imaging experiments.

Ca2+ imaging. TGM neurons from non-tumor and tumor-bearing animals (n=4-6 mice/condition) were imaged on the same day. Neurons were incubated with the calcium indicator, Fluo-4AM, at 37°C for 20 min. After dye loading, the cells were washed, and Live Cell Imaging Solution (Thermo-Fisher) with 20 mM glucose was added. Calcium imaging was conducted at room temperature. Changes in intracellular Ca^{2+} were measured using a Nikon scanning confocal microscope with a□10x objective. Fluo-4AM was excited at 488 nm using an argon laser with intensity attenuated to 1%. The fluorescence images were acquired in the confocal frame (1024□×□1024 pixels) scan mode. After 1 min of baseline measure, capsaicin (300nM final concentration) was added. Ca^{2+} images were recorded before, during and after capsaicin application. Image acquisition and analysis were achieved using NIS-Elements imaging software. Fluo-4AM responses were standardized and shown as percent change from the initial frame. Data are presented as the relative change in fluorescence ($\Delta F/F_0$), where F_0 is the basal fluorescence and $\Delta F=F-F_0$ with F being the measured intensity recorded during the experiment. Calcium responses were analyzed only for neurons responding to ionomycin (10

μM, positive control) to ensure neuronal health. Treatment with the cell permeable Ca^{2+} chelator, BAPTA (200 μM), served as a negative control.

Stereotaxic AAV injection. Male mice were anesthetized with 2% isoflurane and placed in a stereotaxic head frame on a heating pad. A midline incision was made down the scalp and a craniotomy was made using a micro drill. A 10-μl Hamilton syringe was used to infuse 1 μl of AAV1/Syn-GCaMP6f-WPRESV40 (titer 4.65×10^{13} GC per ml, via Addgene) into the parabrachial nucleus (−5.3 mm anteroposterior, -1.3 mm mediolateral, −3 mm dorsoventral) via a microsyringe pump. After infusion, the needle was kept at the injection site for 5 min and then slowly withdrawn. Two weeks following stereotaxic surgeries, tumors were introduced by implanting MOC2-7 cells orthotopically into the oral cavity as described above.

***Ex vivo* Ca2+ imaging of brain slices.** Two weeks post-tumor (or sham) implantation, wildtype and tumor-bearing mice (n=3 mice/group) were anesthetized under isoflurane and perfused intracardially with 10 ml of ice-cold N-methyl-d-glucamine (NMDG) solution [92 mM NMDG, 30 mM $NaHCO_3$, 25 mM glucose, 20 mM Hepes, 10 mM $MgSO_4$, 5 mM sodium ascorbate, 3 mM sodium pyruvate, 2.5 mM KCl, 2 mM thiourea, 1.25 mM NaH_2PO_4, and 0.5 mM $CaCl_2$ (pH 7.3, 300 mOsm, bubbled with 95% O2 and 5% CO_2)] [36]. The brains were quickly removed and placed into additional ice-cold NMDG solution for slicing. Coronal slices (150μm) were cut using a vibratome (n=3 slices/brain). Slices were transferred to Hepes holding solution and warmed to 37°C (bubbled with 95% O_2 and 5% CO_2) for 1 hour. After incubation, slices were transferred to the recording chamber with RT (22° to 25°C) recording solution. A miniaturized microscope (Miniscope V4) imaged the GCaMP6f signal from the slices. Each video was

processed with motion correction and ΔF/F calculation. Regions of interest (ROIs; considered as a single cell soma) were manually selected. ROIs that exhibited short bursts of ΔF/F changes or fluctuations during the recording were analyzed. The ΔF/F changes were then aligned with the time window of treatment. Movement correction was performed using the motion correction module in the EZcalcium toolbox employed in MATLAB [37]. The fluorescence intensity trace of each neuron was extracted, and ΔF/F was calculated (CNMF).

Statistical analysis. GraphPad Prism (version 10.0.3, 2023) was utilized for all statistical analyses.

Gene expression: For qRT-PCR analysis, Ct values for each gene were normalized to that of the reference gene. Statistical analysis by multiple student's t-test.

Ca^{2+} imaging: Statistical analysis by unpaired student's t-test. Fluo-4AM/GCaMP6f responses were standardized and shown as percent change from the initial frame. Data are presented as the relative change in fluorescence ($\Delta F/F_0$), where F_0 is the basal fluorescence and $\Delta F=F-F_0$ with F being the peak response.

Western blot: Membranes were visualized, and proteins were quantified using the Odyssey infrared imaging system and software (Li-COR). Densitometric quantification of western blots was performed by normalizing the signal from tumor or non-tumor ganglia to the β-actin (loading control) signal and differences assessed by one-way ANOVA with post-hoc Tukey test.

Fos brain immunostaining: The numbers of Fos (cFos, ΔFosB) immune-positive neurons in brain sections from tumor-bearing or non-tumor animals were quantified as described above and statistically analyzed by 2-way ANOVA with multiple comparisons.

Nesting scores: The variations over time of the nesting scores for each group were statistically analyzed by repeated measures ANOVA. Exclusion criteria of an average baseline score of 3 or greater was used to ensure all mice were good nest builders.

Time to interact scores (cookie test): Statistical analysis by repeated measures ANOVA.

Voluntary wheel running: The data were collected in 1-minute bins continuously. When compiling the data, the sum of bins between 8pm to 8am is taken for each individual animal for voluntary nightly running. Baseline is calculated by taking the final 3 days prior to tumor implantation and averaging the values. The percent change is then calculated for each day from baseline for each mouse. The data were then analyzed using a repeated measures 2-way ANOVA.

Food disappearance: Statistical analysis by repeated measures ANOVA.

Weight: Statistical analysis by repeated measures ANOVA.

Tumor growth curves: Statistical analysis of tumor growth curves by repeated measures ANOVA

Kaplan Meier survival: Statistical analysis of survival by Log-rank (Mantel-Cox) test.

References

1 Carreira, H. *et al.* Associations Between Breast Cancer Survivorship and Adverse Mental Health Outcomes: A Systematic Review. *Journal of the National Cancer Institute* **110**, 1311-1327 (2018). https://doi.org:10.1093/jnci/djy177

2 Pitman, A., Suleman, S., Hyde, N. & Hodgkiss, A. Depression and anxiety in patients with cancer. *Bmj* **361**, k1415 (2018). https://doi.org:10.1136/bmj.k1415

3 Walker, J. *et al.* Prevalence of depression in adults with cancer: a systematic review. *Annals of oncology : official journal of the European Society for Medical Oncology* **24**, 895-900 (2013). https://doi.org:10.1093/annonc/mds575

4 Zhu, J. *et al.* First-onset mental disorders after cancer diagnosis and cancer-specific mortality: a nationwide cohort study. *Annals of oncology : official journal of the European Society for Medical Oncology* **28**, 1964-1969 (2017). https://doi.org:10.1093/annonc/mdx265

5 Steel, Z. *et al.* The global prevalence of common mental disorders: a systematic review and meta-analysis 1980-2013. *Int J Epidemiol* **43**, 476-493 (2014). https://doi.org:10.1093/ije/dyu038

6 Gotze, H. *et al.* Depression and anxiety in long-term survivors 5 and 10 years after cancer diagnosis. *Supportive care in cancer : official journal of the Multinational Association of Supportive Care in Cancer* **28**, 211-220 (2020). https://doi.org:10.1007/s00520-019-04805-1

7 Kuba, K. *et al.* Risk for depression and anxiety in long-term survivors of hematologic cancer. *Health Psychol* **38**, 187-195 (2019). https://doi.org:10.1037/hea0000713

8 Wang, Y. H. *et al.* Depression and anxiety in relation to cancer incidence and mortality: a systematic review and meta-analysis of cohort studies. *Mol Psychiatry* **25**, 1487-1499 (2020). https://doi.org:10.1038/s41380-019-0595-x

9 Naser, A. Y. *et al.* Depression and Anxiety in Patients With Cancer: A Cross-Sectional Study. *Front Psychol* **12**, 585534 (2021). https://doi.org:10.3389/fpsyg.2021.585534

10 Tsaras, K. *et al.* Assessment of Depression and Anxiety in Breast Cancer Patients: Prevalence and Associated Factors. *Asian Pacific journal of cancer prevention : APJCP* **19**, 1661-1669 (2018). https://doi.org:10.22034/APJCP.2018.19.6.1661

11 Madeo, M. *et al.* Cancer exosomes induce tumor innervation. *Nature communications* **9**, 4284 (2018). https://doi.org:10.1038/s41467-018-06640-0

12 Lucido, C. T. *et al.* Innervation of cervical carcinoma is mediated by cancer-derived exosomes. *Gynecologic oncology* (2019). https://doi.org:10.1016/j.ygyno.2019.04.651

13 Barr, J. L. *et al.* Intra-Tumoral Nerve-Tracing in a Novel Syngeneic Model of High-Grade Serous Ovarian Carcinoma. *Cells* **10** (2021). https://doi.org:10.3390/cells10123491

14 Renz, B. W. *et al.* beta2 Adrenergic-Neurotrophin Feedforward Loop Promotes Pancreatic Cancer. *Cancer cell* **33**, 75-90 e77 (2018). https://doi.org:10.1016/j.ccell.2017.11.007

15 Hayakawa, Y. *et al.* Nerve Growth Factor Promotes Gastric Tumorigenesis through Aberrant Cholinergic Signaling. *Cancer cell* **31**, 21-34 (2017). https://doi.org:10.1016/j.ccell.2016.11.005

16 Wang, K. *et al.* The neurotrophic factor neurturin contributes toward an aggressive cancer cell phenotype, neuropathic pain and neuronal plasticity in pancreatic cancer. *Carcinogenesis* **35**, 103-113 (2014). https://doi.org:10.1093/carcin/bgt312

17 Kasprzak, A. & Adamek, A. The Neuropeptide System and Colorectal Cancer Liver Metastases: Mechanisms and Management. *International journal of molecular sciences* **21** (2020). https://doi.org:10.3390/ijms21103494

18 Silverman, D. A. *et al.* Cancer-Associated Neurogenesis and Nerve-Cancer Cross-talk. *Cancer research* **81**, 1431-1440 (2021). https://doi.org:10.1158/0008-5472.CAN-20-2793

19 Cole, S. W., Nagaraja, A. S., Lutgendorf, S. K., Green, P. A. & Sood, A. K. Sympathetic nervous system regulation of the tumour microenvironment. *Nature reviews. Cancer* **15**, 563-572 (2015). https://doi.org:10.1038/nrc3978

20 Magnon, C. *et al.* Autonomic nerve development contributes to prostate cancer progression. *Science* **341**, 1236361 (2013). https://doi.org:10.1126/science.1236361

21 Sadighparvar, S., Darband, S. G., Ghaderi-Pakdel, F., Mihanfar, A. & Majidinia, M. Parasympathetic, but not sympathetic denervation, suppressed colorectal cancer progression. *Eur J Pharmacol* **913**, 174626 (2021). https://doi.org:10.1016/j.ejphar.2021.174626

22 Chen, D. & Ayala, G. E. Innervating Prostate Cancer. *The New England journal of medicine* **378**, 675-677 (2018). https://doi.org:10.1056/NEJMcibr1714003

23 Kamiya, A. *et al.* Genetic manipulation of autonomic nerve fiber innervation and activity and its effect on breast cancer progression. *Nature neuroscience* **22**, 1289-1305 (2019). https://doi.org:10.1038/s41593-019-0430-3

24 Chen, M. *et al.* The Rostral Ventromedial and Lateral Medulla Are the Major Areas Responsive to Lung Cancer Progression among Brainstem Lung-Innervating Nuclei. *Brain Sci* **12** (2022). https://doi.org:10.3390/brainsci12111486

25 Henry, M. *et al.* Psychosocial outcomes of human papillomavirus (HPV)- and non-HPV-related head and neck cancers: A longitudinal study. *Psychooncology* **31**, 185-197 (2022). https://doi.org:10.1002/pon.5803

26 Virgen, C. G. *et al.* Pharmacological management of cancer pain: Novel therapeutics. *Biomed Pharmacother* **156**, 113871 (2022). https://doi.org:10.1016/j.biopha.2022.113871

27 Hjermstad, M. J., Fainsinger, R., Kaasa, S. & European Palliative Care Research, C. Assessment and classification of cancer pain. *Curr Opin Support Palliat Care* **3**, 24-30 (2009). https://doi.org:10.1097/SPC.0b013e3283260644

28 van den Beuken-van Everdingen, M. H. *et al.* Prevalence of pain in patients with cancer: a systematic review of the past 40 years. *Annals of oncology : official journal of the European Society for Medical Oncology* **18**, 1437-1449 (2007). https://doi.org:10.1093/annonc/mdm056

29 Judd, N. P. *et al.* ERK1/2 regulation of CD44 modulates oral cancer aggressiveness. *Cancer research* **72**, 365-374 (2012). https://doi.org:10.1158/0008-5472.CAN-11-1831

30 Onken, M. D. *et al.* A surprising cross-species conservation in the genomic landscape of mouse and human oral cancer identifies a transcriptional signature predicting metastatic disease. *Clinical cancer research : an official journal of the American Association for Cancer Research* **20**, 2873-2884 (2014). https://doi.org:10.1158/1078-0432.CCR-14-0205

31 Cavanaugh, D. J. *et al.* Trpv1 reporter mice reveal highly restricted brain distribution and functional expression in arteriolar smooth muscle cells. *The Journal of neuroscience : the official journal of the Society for Neuroscience* **31**, 5067-5077 (2011). https://doi.org:10.1523/JNEUROSCI.6451-10.2011

32 Neely, C. L. C., Pedemonte, K. A., Boggs, K. N. & Flinn, J. M. Nest Building Behavior as an Early Indicator of Behavioral Deficits in Mice. *Journal of visualized experiments : JoVE* (2019). https://doi.org:10.3791/60139

33 Deacon, R. M. Assessing nest building in mice. *Nature protocols* **1**, 1117-1119 (2006). https://doi.org:10.1038/nprot.2006.170

34 Kraeuter, A. K., Guest, P. C. & Sarnyai, Z. The Nest Building Test in Mice for Assessment of General Well-Being. *Methods in molecular biology* **1916**, 87-91 (2019). https://doi.org:10.1007/978-1-4939-8994-2_7

35 Kee, N., Teixeira, C. M., Wang, A. H. & Frankland, P. W. Imaging activation of adult-generated granule cells in spatial memory. *Nature protocols* **2**, 3033-3044 (2007). https://doi.org:10.1038/nprot.2007.415

36 Ting, J. T. *et al.* Preparation of Acute Brain Slices Using an Optimized N-Methyl-D-glucamine Protective Recovery Method. *Journal of visualized experiments : JoVE* (2018). https://doi.org:10.3791/53825

37 Cantu, D. A. *et al.* EZcalcium: Open-Source Toolbox for Analysis of Calcium Imaging Data. *Front Neural Circuits* **14**, 25 (2020). https://doi.org:10.3389/fncir.2020.00025

38 Restaino, A. C. *et al.* Functional neuronal circuits promote disease progression in cancer. *Sci Adv* **9**, eade4443 (2023). https://doi.org:10.1126/sciadv.ade4443

39 Menezes, F. D. S., Fernandes, G. A., Antunes, J. L. F., Villa, L. L. & Toporcov, T. N. Global incidence trends in head and neck cancer for HPV-related and -unrelated subsites: A systematic review of population-based studies. *Oral oncology* **115**, 105177 (2021). https://doi.org:10.1016/j.oraloncology.2020.105177

40 Georgieff, I. S. *et al.* Expression of high molecular weight tau in the central and peripheral nervous systems. *Journal of cell science* **105 (Pt 3)**, 729-737 (1993). https://doi.org:10.1242/jcs.105.3.729

41 Dellarole, A. & Grilli, M. Adult dorsal root ganglia sensory neurons express the early neuronal fate marker doublecortin. *J Comp Neurol* **511**, 318-328 (2008). https://doi.org:10.1002/cne.21845

42 Bernreuther, C., Salein, N., Matschke, J. & Hagel, C. Expression of doublecortin in tumours of the central and peripheral nervous system and in human non-neuronal tissues. *Acta Neuropathol* **111**, 247-254 (2006). https://doi.org:10.1007/s00401-006-0038-z

43 Borges, L. F. & Sidman, R. L. Axonal transport of lectins in the peripheral nervous system. *The Journal of neuroscience : the official journal of the Society for Neuroscience* **2**, 647-653 (1982).

44 van der Want, J. J., Klooster, J., Cardozo, B. N., de Weerd, H. & Liem, R. S. Tract-tracing in the nervous system of vertebrates using horseradish peroxidase and its conjugates: tracers, chromogens and stabilization for light and electron microscopy. *Brain Res Brain Res Protoc* **1**, 269-279 (1997). https://doi.org:10.1016/s1385-299x(96)00042-6

45 McNicholas, K. & Michael, M. Z. Immuno-characterization of Exosomes Using Nanoparticle Tracking Analysis. *Methods in molecular biology* **1545**, 35-42 (2017). https://doi.org:10.1007/978-1-4939-6728-5_3

46 Dumas, M., Schwab, M. E. & Thoenen, H. Retrograde axonal transport of specific macromolecules as a tool for characterizing nerve terminal membranes. *Journal of neurobiology* **10**, 179-197 (1979). https://doi.org:10.1002/neu.480100207

47 Sillitoe, R. V. Mossy Fibers Terminate Directly Within Purkinje Cell Zones During Mouse Development. *Cerebellum* **15**, 14-17 (2016). https://doi.org:10.1007/s12311-015-0712-6

48 Tabuchi, K. *et al.* GAL4/UAS-WGA system as a powerful tool for tracing Drosophila transsynaptic neural pathways. *Journal of neuroscience research* **59**, 94-99 (2000).
49 Levy, S. L., White, J. J., Lackey, E. P., Schwartz, L. & Sillitoe, R. V. WGA-Alexa Conjugates for Axonal Tracing. *Current protocols in neuroscience* **79**, 1 28 21-21 28 24 (2017). https://doi.org:10.1002/cpns.28
50 Itaya, S. K. Anterograde transsynaptic transport of WGA-HRP in rat olfactory pathways. *Brain research* **409**, 205-214 (1987). https://doi.org:10.1016/0006-8993(87)90703-7
51 Itaya, S. K., Van Hoesen, G. W. & Barnes, C. L. Anterograde transsynaptic transport of WGA-HRP in the limbic system of rat and monkey. *Brain research* **398**, 397-402 (1986). https://doi.org:10.1016/0006-8993(86)91504-0
52 Carson, K. A. & Mesulam, M. M. Ultrastructural evidence in mice that transganglionically transported horseradish peroxidase-wheat germ agglutinin conjugate reaches the intraspinal terminations of sensory neurons. *Neuroscience letters* **29**, 201-206 (1982). https://doi.org:10.1016/0304-3940(82)90317-2
53 Yeh, L. F., Watanabe, M., Sulkes-Cuevas, J. & Johansen, J. P. Dysregulation of aversive signaling pathways: a novel circuit endophenotype for pain and anxiety disorders. *Curr Opin Neurobiol* **48**, 37-44 (2018). https://doi.org:10.1016/j.conb.2017.09.006
54 Hu, H. Reward and Aversion. *Annual review of neuroscience* **39**, 297-324 (2016). https://doi.org:10.1146/annurev-neuro-070815-014106
55 Zhu, Y. B. *et al.* PBN-PVT projections modulate negative affective states in mice. *eLife* **11** (2022). https://doi.org:10.7554/eLife.68372
56 Russo, S. J. & Nestler, E. J. The brain reward circuitry in mood disorders. *Nature reviews. Neuroscience* **14**, 609-625 (2013). https://doi.org:10.1038/nrn3381
57 Balood, M. *et al.* Nociceptor neurons affect cancer immunosurveillance. *Nature* (2022). https://doi.org:10.1038/s41586-022-05374-w
58 Michetti, F. *et al.* The S100B story: from biomarker to active factor in neural injury. *Journal of neurochemistry* **148**, 168-187 (2019). https://doi.org:10.1111/jnc.14574
59 Liu, Q. *et al.* Transcriptional Alterations of Mouse Trigeminal Ganglion Neurons Following Orofacial Inflammation Revealed by Single-Cell Analysis. *Frontiers in cellular neuroscience* **16**, 885569 (2022). https://doi.org:10.3389/fncel.2022.885569
60 Malin, S. A., Davis, B. M. & Molliver, D. C. Production of dissociated sensory neuron cultures and considerations for their use in studying neuronal function and plasticity. *Nature protocols* **2**, 152-160 (2007). https://doi.org:10.1038/nprot.2006.461
61 Ortiz-Renteria, M. *et al.* TRPV1 channels and the progesterone receptor Sig-1R interact to regulate pain. *Proceedings of the National Academy of Sciences of the United States of America* **115**, E1657-E1666 (2018). https://doi.org:10.1073/pnas.1715972115
62 Bhave, G. *et al.* Protein kinase C phosphorylation sensitizes but does not activate the capsaicin receptor transient receptor potential vanilloid 1 (TRPV1). *Proceedings of the National Academy of Sciences of the United States of America* **100**, 12480-12485 (2003). https://doi.org:10.1073/pnas.2032100100
63 Numazaki, M. *et al.* Structural determinant of TRPV1 desensitization interacts with calmodulin. *Proceedings of the National Academy of Sciences of the United States of America* **100**, 8002-8006 (2003). https://doi.org:10.1073/pnas.1337252100
64 Numazaki, M., Tominaga, T., Toyooka, H. & Tominaga, M. Direct phosphorylation of capsaicin receptor VR1 by protein kinase Cepsilon and identification of two target serine

residues. *The Journal of biological chemistry* **277**, 13375-13378 (2002). https://doi.org:10.1074/jbc.C200104200

65 Bhave, G. *et al.* cAMP-dependent protein kinase regulates desensitization of the capsaicin receptor (VR1) by direct phosphorylation. *Neuron* **35**, 721-731 (2002). https://doi.org:10.1016/s0896-6273(02)00802-4

66 Scheff, N. N. *et al.* Oral cancer induced TRPV1 sensitization is mediated by PAR(2) signaling in primary afferent neurons innervating the cancer microenvironment. *Scientific reports* **12**, 4121 (2022). https://doi.org:10.1038/s41598-022-08005-6

67 Chung, L. A Brief Introduction to the Transduction of Neural Activity into Fos Signal. *Dev Reprod* **19**, 61-67 (2015). https://doi.org:10.12717/DR.2015.19.2.061

68 Hudson, A. E. Genetic Reporters of Neuronal Activity: c-Fos and G-CaMP6. *Methods in enzymology* **603**, 197-220 (2018). https://doi.org:10.1016/bs.mie.2018.01.023

69 Nestler, E. J., Barrot, M. & Self, D. W. DeltaFosB: a sustained molecular switch for addiction. *Proceedings of the National Academy of Sciences of the United States of America* **98**, 11042-11046 (2001). https://doi.org:10.1073/pnas.191352698

70 Nestler, E. J., Kelz, M. B. & Chen, J. DeltaFosB: a molecular mediator of long-term neural and behavioral plasticity. *Brain research* **835**, 10-17 (1999). https://doi.org:10.1016/s0006-8993(98)01191-3

71 Chen, T. W. *et al*. Ultrasensitive fluorescent proteins for imaging neuronal activity. *Nature* **499**, 295-300 (2013). https://doi.org:10.1038/nature12354

72 Niedzwiedz, C. L., Knifton, L., Robb, K. A., Katikireddi, S. V. & Smith, D. J. Depression and anxiety among people living with and beyond cancer: a growing clinical and research priority. *BMC cancer* **19**, 943 (2019). https://doi.org:10.1186/s12885-019-6181-4

73 Utley, M., Adeyanju, T., Bernardo, B., Paskett, E. D. & Krok-Schoen, J. L. The association between mental health, social support and physical health outcomes among older female cancer survivors. *J Geriatr Oncol* **13**, 834-838 (2022). https://doi.org:10.1016/j.jgo.2022.04.001

74 Ji, X. *et al.* National estimates of mental health service use and unmet needs among adult cancer survivors. *Cancer* **127**, 4296-4305 (2021). https://doi.org:10.1002/cncr.33827

75 Mishra, S. K., Tisel, S. M., Orestes, P., Bhangoo, S. K. & Hoon, M. A. TRPV1-lineage neurons are required for thermal sensation. *The EMBO journal* **30**, 582-593 (2011). https://doi.org:10.1038/emboj.2010.325

76 Liu, M. Y. *et al.* Sucrose preference test for measurement of stress-induced anhedonia in mice. *Nature protocols* **13**, 1686-1698 (2018). https://doi.org:10.1038/s41596-018-0011-z

77 Eliwa, H. *et al.* Adult neurogenesis augmentation attenuates anhedonia and HPA axis dysregulation in a mouse model of chronic stress and depression. *Psychoneuroendocrinology* **124**, 105097 (2021). https://doi.org:10.1016/j.psyneuen.2020.105097

78 Norden, D. M. *et al*. Tumor growth increases neuroinflammation, fatigue and depressive-like behavior prior to alterations in muscle function. *Brain, behavior, and immunity* **43**, 76-85 (2015). https://doi.org:10.1016/j.bbi.2014.07.013

79 Zombeck, J. A., Fey, E. G., Lyng, G. D. & Sonis, S. T. A clinically translatable mouse model for chemotherapy-related fatigue. *Comp Med* **63**, 491-497 (2013).

80 Grossberg, A. J. *et al.* Tumor-Associated Fatigue in Cancer Patients Develops Independently of IL1 Signaling. *Cancer research* **78**, 695-705 (2018). https://doi.org:10.1158/0008-5472.CAN-17-2168

81 Bower, J. E. *et al.* Inflammation and behavioral symptoms after breast cancer treatment: do fatigue, depression, and sleep disturbance share a common underlying mechanism? *Journal of clinical oncology : official journal of the American Society of Clinical Oncology* **29**, 3517-3522 (2011). https://doi.org:10.1200/JCO.2011.36.1154

82 Norden, D. M. *et al.* Fluoxetine prevents the development of depressive-like behavior in a mouse model of cancer related fatigue. *Physiol Behav* **140**, 230-235 (2015). https://doi.org:10.1016/j.physbeh.2014.12.045

83 Chen, A. M. *et al.* Depression among long-term survivors of head and neck cancer treated with radiation therapy. *JAMA Otolaryngol Head Neck Surg* **139**, 885-889 (2013). https://doi.org:10.1001/jamaoto.2013.4072

84 Lazure, K. E., Lydiatt, W. M., Denman, D. & Burke, W. J. Association between depression and survival or disease recurrence in patients with head and neck cancer enrolled in a depression prevention trial. *Head & neck* **31**, 888-892 (2009). https://doi.org:10.1002/hed.21046

85 Elaldi, R. *et al.* Correlations between long-term quality of life and patient needs and concerns following head and neck cancer treatment and the impact of psychological distress. A multicentric cross-sectional study. *European archives of oto-rhino-laryngology : official journal of the European Federation of Oto-Rhino-Laryngological Societies* **278**, 2437-2445 (2021). https://doi.org:10.1007/s00405-020-06326-8

86 Navratilova, E. *et al.* Positive emotions and brain reward circuits in chronic pain. *J Comp Neurol* **524**, 1646-1652 (2016). https://doi.org:10.1002/cne.23968

87 Mercer Lindsay, N., Chen, C., Gilam, G., Mackey, S. & Scherrer, G. Brain circuits for pain and its treatment. *Science translational medicine* **13**, eabj7360 (2021). https://doi.org:10.1126/scitranslmed.abj7360

88 Backes, T. M. *et al.* Stimulation of TRPV1 channels activates the AP-1 transcription factor. *Biochemical pharmacology* **150**, 160-169 (2018). https://doi.org:10.1016/j.bcp.2018.02.008

89 Boedtkjer, E. & Pedersen, S. F. The Acidic Tumor Microenvironment as a Driver of Cancer. *Annual review of physiology* (2019). https://doi.org:10.1146/annurev-physiol-021119-034627

90 Pocock, R. & Hobert, O. Oxygen levels affect axon guidance and neuronal migration in Caenorhabditis elegans. *Nature neuroscience* **11**, 894-900 (2008). https://doi.org:10.1038/nn.2152

91 Pocock, R. & Hobert, O. Hypoxia activates a latent circuit for processing gustatory information in C. elegans. *Nature neuroscience* **13**, 610-614 (2010). https://doi.org:10.1038/nn.2537

92 Stevenson, T. J. *et al.* Hypoxia disruption of vertebrate CNS pathfinding through ephrinB2 Is rescued by magnesium. *PLoS Genet* **8**, e1002638 (2012). https://doi.org:10.1371/journal.pgen.1002638

93 Amit, M. *et al.* Loss of p53 drives neuron reprogramming in head and neck cancer. *Nature* **578**, 449-454 (2020). https://doi.org:10.1038/s41586-020-1996-3

94 Ueda, H. R. *et al.* Whole-Brain Profiling of Cells and Circuits in Mammals by Tissue Clearing and Light-Sheet Microscopy. *Neuron* **106**, 369-387 (2020). https://doi.org:10.1016/j.neuron.2020.03.004

95 Kobayashi, K. *et al.* Distinct expression of TRPM8, TRPA1, and TRPV1 mRNAs in rat primary afferent neurons with adelta/c-fibers and colocalization with trk receptors. *J Comp Neurol* **493**, 596-606 (2005). https://doi.org:10.1002/cne.20794

96 Mickle, A. D., Shepherd, A. J. & Mohapatra, D. P. Sensory TRP channels: the key transducers of nociception and pain. *Prog Mol Biol Transl Sci* **131**, 73-118 (2015). https://doi.org:10.1016/bs.pmbts.2015.01.002

97 Renna, M. E. *et al.* Depression and anxiety in colorectal cancer patients: Ties to pain, fatigue, and inflammation. *Psychooncology* **31**, 1536-1544 (2022). https://doi.org:10.1002/pon.5986

98 Walker, A. K., Kavelaars, A., Heijnen, C. J. & Dantzer, R. Neuroinflammation and comorbidity of pain and depression. *Pharmacological reviews* **66**, 80-101 (2014). https://doi.org:10.1124/pr.113.008144

99 Grossberg, A. J. *et al.* Interleukin 6-independent metabolic reprogramming as a driver of cancer-related fatigue. *Brain, behavior, and immunity* **88**, 230-241 (2020). https://doi.org:10.1016/j.bbi.2020.05.043

100 Thaker, P. H. *et al.* Chronic stress promotes tumor growth and angiogenesis in a mouse model of ovarian carcinoma. *Nature medicine* **12**, 939-944 (2006). https://doi.org:10.1038/nm1447

101 Kim-Fuchs, C. *et al.* Chronic stress accelerates pancreatic cancer growth and invasion: a critical role for beta-adrenergic signaling in the pancreatic microenvironment. *Brain, behavior, and immunity* **40**, 40-47 (2014). https://doi.org:10.1016/j.bbi.2014.02.019

102 Yap, E. L. & Greenberg, M. E. Activity-Regulated Transcription: Bridging the Gap between Neural Activity and Behavior. *Neuron* **100**, 330-348 (2018). https://doi.org:10.1016/j.neuron.2018.10.013

103 Takayanagi-Kiya, S. & Kiya, T. Activity-dependent visualization and control of neural circuits for courtship behavior in the fly Drosophila melanogaster. *Proceedings of the National Academy of Sciences of the United States of America* **116**, 5715-5720 (2019). https://doi.org:10.1073/pnas.1814628116

Acknowledgments: We thank the Histology and Imaging Core (Sanford Research, supported by National Institutes of Health, National Institute of General Medical Sciences, Center of Biomedical Research Excellence 5P20GM103548 and P30GM145398), specifically Claire Evans who provided her services and expertise towards this project. We also thank the following funding sources for their critical contributions to this work: National Institutes of Health, National Institute of Dental and Craniofacial Research grant 1R01DE032712-01 (PDV),

Institutional Development Award (IDeA) from the National Institute of General Medical Sciences of the National Institutes of Health grant 5P20GM103548 (PDV). DaCCoTA Scholar Award supported by the National Institute of General Medical Sciences of the National Institutes of Health grant U54 GM128729 (PDV). National Institute of Health, National Cancer Institute grant R37 1R37CA242006-01A1 (MA). Stiefel family Discovery award (MA). Institutional Research Grant (MA). Disruptive Science Moonshot award, MDACC (MA). Canadian Institutes of Health Research grants 162211, 461274, 461275 (ST). National Institutes of Health (R01 CA193522; R21 NS130712) (RD).

Materials & Correspondence: Correspondence and material requests should be addressed to Paola D. Vermeer: Paola.Vermeer@sanfordhealth.org

Data availability statement: Data will be available upon reasonable request.

Fig 1. Tumor-infiltrating nerves form a circuit connecting to the brain. (**A**) Western blot of MOC2-7 whole tumor lysates for Tau (**A**) and Doublecortin, DCX (**B**). Tumors were harvested at different time points (as indicated) post-tumor implantation (n=3 mice/time point). Mouse brain, positive control; MOC2-7, whole cell lysate control; β-actin, loading control. Immunohistochemical staining for β-III tubulin (β3T, brown, arrows) of tumors harvested on days 4 (**C**), 10 (**D**) and 20 (**E**) post tumor implantation. Scale bar, 100 µm. Dotted boxes are shown at higher magnification below each panel; scale bar, 50µm. Arrows highlight positive nerves staining. Representative *en face* confocal image of WGA positive (red) neurites within tumor (**F**) and the ipsilateral trigeminal ganglion (**G**) from a mouse orthotopically implanted with a MOC2-7 tumor and intra-tumorally injected with the tracer. Scale bars, 200µm. (**H**) Low magnification section of ipsilateral and contralateral TGM ganglia from a MOC2-7 tumor-bearing mouse that was intra-tumorally injected with WGA. The V3 branch of the TGM is marked with an arrow. WGA (red) positive neurons found only in the ipsilateral TGM. Scale bar, 500 µm. (**I**) Compressed Z-stack of confocal images demonstrating restricted WGA (red) within the tumor bed (cytokeratin, green). Vertical and horizontal cross-sections highlight that WGA (red) localizes strictly within the tumor (green) and does not leak out. Yellow shows the merged file. (**J**) Diagram showing the location of the trigeminal (TGM) ganglion, extension of its neurites into the tumor bed and the existing circuit which includes the spinal nucleus of the TGM (SpVc), the parabrachial nucleus (PBN) and the central amygdala (CeA) which get labeled following WGA injection into tumor. (**K**) Representative confocal images of the SpVc, PBN and CeA following injection of 2 µl of WGA into an oral MOC2-7 tumor (n=10 mice). Representative confocal images of SpVc, PBN and CeA following injection of (**L**) 10 µl (n=3

mice) of WGA into the oral cavity of a non-tumor bearing control animal. Scale bar, 50 μm. WGA (red looks pink due to DaPi), DaPi nuclear counterstain (blue).

Fig 2. Tumor-infiltrating neurons become transcriptionally and functionally altered. Trigeminal (TGM) ganglia from tumor bearing (red) or non-tumor bearing (blue) mice were analyzed by (**A**) quantitative PCR array. N=4 TGM/group from n=4 mice/group; n=4 arrays/group. Ct values for each gene normalized to that of a housekeeping gene. Statistical analysis by multiple students t-test. *, $p<0.05$; **, $p<0.01$; ***, $p<0.001$, ****, $p<0.00001$. Data are expressed as means ± standard deviation. (**B**) Representative fluorescent images of dissociated neurons from the ipsilateral or contralateral TGM ganglia from a MOC2-7 tumor-bearing mouse. N=6 of each ganglia harvested from 6 tumor-bearing animals with n= 4-8 neurons analyzed/ganglia. The color palette reflects the strength of the calcium signal. Images are taken pre- and post-treatment with capsaicin. (**C**) Graph of average change in fluorescence for all neurons analyzed in each group (ipsilateral and contralateral). Statistical analysis by student's t-test. Arrow, time of capsaicin (300 nM) stimulation. Graph of average peak of the curve (**D**) and area under the curve (**E**) from panel C. Statistical analysis by student's t-test. **, $p<0.01$. (**F**) Quantification of Ca^{+2} responses to capsaicin (300 nM) from non-tumoral (Control) and tumor-infiltrating, $tracer^{+}$ (Tumor-infiltrating) neurons. N= 4-8 neurons/group from n=4 control and n=7 tumor-bearing mice. Statistical analysis by paired students t-test, *, $p<0.05$. Data expressed as means ± SEM. (**G**) Representative western blot of trigeminal ganglia from non-tumor (N) or MOC2-7 tumor-bearing (T) animals for phosphorylated TRPV1 (pTRPV1, Ser502, Ser800), σ1 receptor (σ1R) and β-actin (loading control). Densitometric quantification of western blots for pTRPV1 (**H**) and σ1R (**I**). Statistical analysis by student's t-test. *, $p< 0.05$. Data are expressed as means ± SEM. (n=3-4 mice/group).

Fig 3. Elevated CNS neuronal activity in tumor bearing mice. Representative fluorescent photomicrographs of the spinal nucleus of the TGM (SpVc) (**A**), parabrachial nucleus (PBN) (**B**) and central amygdala (CeA) (**C**) from a control (-tumor) and MOC2-7 tumor-bearing (+tumor) mouse brains immuonfluorescently stained for cFos (red) or ΔFosB (green). Nuclei counterstained with DaPi (blue). Dotted circle denotes each brain region. Scale bar, 100 μm. Brain landmarks: Spc, superior cerebellar peduncle; VL, lateral ventricle; IA, intercalated amygdalar nucleus. Quantification of cFos and ΔFosB staining in SpVc (**D**), PBN (**E**) and CeA (**F**) from control (-tumor) and tumor-bearing (+tumor) mice. N= 4 mice/group with n=2-4 sections analyzed/brain region/mouse/group. Data are expressed as the mean ± SEM. Statistical analysis by one-way ANOVA*, $p<0.05$; **, $p<0.01$; ***, $p<0.001$; ns, not significant. Scale bar, 100 μm. Representative heat maps of regions of interest (ROI), each of which represent one neuron, within an *ex vivo* brain slice from non-tumor (control) (**G**) and tumor-bearing (**H**) mice. The color palette reflects the strength of the calcium signal. Arrow denotes the time of KCl (30 mM) application. N= 3 mice/group with n=3 slices/brain. Quantification of calcium imaging data from (n= 5 mice/group with n=2-4 sections analyzed/mouse) analyzing the peak of the curve (**I**) and the area under the curve (**J**). Statistical analysis by student's t-test. ****, $p< 0.0001$; ***, p< 001.

Fig 4. Intra-tumoral neurons impact behavior. (**A**) Bright field photomicrograph of TGM ganglion from C57BL/6 or $TRPV1^{cre}$::$DTA^{fl/wt}$ mice IHC stained for TRPV1 (brown). Scale bar, 100μm. Quantification of cFos and ΔFosB from the brains of C57Bl/6 (C57) or $TRPV1^{cre}$::$DTA^{fl/wt}$ (DTA) animals with MOC2-7 oral tumors in the Spinal nucleus of the

trigeminal (SpVc) (**B**), the parabrachial nucleus (PBN) (**C**) and the central amygdala (CeA) (**D**). N=4 mice/group with n=2-4 sections analyzed/brain region/mouse. Statistical analysis by one-way ANOVA. **, $p<0.01$; ***, $p<0.001$. Data displayed as mean ± SEM. C57BL/6 (black, n=15) and TRPV1^{cre}::DTA$^{fl/wt}$ (blue, n=14) mice were orthotopically implanted with MOC2-7 tumor and behavior assessed weekly and statistically analyzed by repeated measures ANOVA. (**E**) Graph of nesting scores over time. There is a main effect of time such that there is a decline in nesting performance over time. We also see a time by strain interaction in that C57BL/6 mice show a greater decline than the nociceptor neuron ablated TRPV1^{cre}::DTA$^{fl/wt}$ mice. Post hoc testing shows a significant difference in nesting on day 27 ($p=0.0315$). (**F**) Graph of time to interact with the cookie in the cookie test. There is a main effect of time such that the time to interact with the cookie declines over time. There is a main effect of strain such that nociceptor neuron ablated TRPV1^{cre}::DTA$^{fl/wt}$ mice were faster to interact with the cookie. Finally, there is a time by strain interaction such that nociceptor neuron ablated TRPV1^{cre}::DTA$^{fl/wt}$ mice showed progressively faster task performance, while in C57BL/6 mice interaction time plateaued. Post hoc testing demonstrates a significant difference between the groups on days 3, 22, and 27 ($p<0.05$). (**G**) Tumor growth curves for mice that underwent behavioral testing. Statistical analysis by repeated measures ANOVA. There is a main effect of time such that there is an increase in tumor volume over time. We also see a time by strain interaction in that C57BL/6 mice have larger tumors than nociceptor ablated TRPV1^{cre}::DTA$^{fl/wt}$ mice. (**H**) Kaplan-Meier survival curve for mice in panel I. Statistical analysis by Log-rank (Mantel-Cox) test. ****, $p<0.0001$. (**I**) Graph of % change in weight from baseline. Dotted line represents baseline. Statistical analysis by repeated measures ANOVA. There was a main effect of time such that both groups showed an initial increase in weight followed by a decrease. Post hoc testing shows

a significant difference between the groups on days 5, 10, and 20. (**J**) Graph of % change from baseline in food consumption. Dotted line represents baseline. Statistical analysis by repeated measures ANOVA. There is a main effect of time such that there is a decline in % food disappearance over time. There is a time by strain interaction such that C57BL/6 mice show a greater decline in % food disappearance compared to nociceptor neuron ablated TRPV1^{cre}::DTA$^{fl/wt}$ mice. In all panels, error bars are SEM.

Fig 5. Denervation of tumors improves behavior, attenuates body weight loss, and reduces tumor growth. (**A**) Graph of nesting scores over time. Statistical analysis by repeated measures ANOVA (group x time): The time factor and its interaction with the group factor are significant with a significant difference between RTX- and vehicle-treated mice on the last time point ($p<0.001$). (**B**) Graph of % change in weight from baseline. Statistical analysis by repeated measures ANOVA (group x time): The time factor and its interaction with the group factor are significant with a significant difference between groups on the last time point ($p<0.01$). (**C**) Tumor volume according to treatment and time: Statistical analysis by repeated measures ANOVA (treatment x time): The time factor and its interaction with the group factor are significant with a significant difference between treatments on the last two time points ($p<0.001$). N=20 mice/group.

Fig 6. Treating for pain does not restore all behaviors. C57BL/6 male mice were orthotopically implanted with MOC2-7 tumors and separated into three groups: carprofen treated (10mg/kg, blue, n=10), buprenorphine treated (3.25mg/kg, red, n=10) or vehicle treated (black, n=9). Mice underwent behavioral testing. All analyses are by repeated measures ANOVA. (**A**) Data are graphed as % of baseline for overnight wheel running. The dotted line represents the baseline. There is a main effect of time such that there is a decline in voluntary wheel running

over time. We also see a time by drug (carprofen) interaction in that vehicle-treated mice show a greater decline in wheel running than carprofen-treated mice. Post hoc testing shows a significant difference in wheel running ($p<0.0001$). (**B**) There is a main effect of time such that there is a decline in voluntary wheel running over time. We also see a time by drug (buprenorphine) interaction in that vehicle-treated mice show a greater decline in wheel running than the buprenorphine-treated mice. Post hoc testing shows a significant difference in wheel running ($p<0.0001$). (**C**) Graph of nesting scores over time. When comparing vehicle vs carprofen groups, there is a main effect of time such that there is a decline in nesting performance over time. We also see a time by drug (carprofen) interaction in that vehicle-treated mice show a greater decline than carprofen-treated mice. Similarly, we see a main effect of time when comparing the vehicle and buprenorphine groups. There is a time by drug (buprenorphine) interaction in that vehicle-treated mice show a greater decline than buprenorphine-treated mice. (**D**) Graph of % change in weight from baseline. The dotted line represents the baseline. There was a main effect of time. There is also a drug (carprofen) by time interaction in that vehicle-treated mice show a greater decline in weight than the carprofen-treated mice. In fact, carprofen treated mice gain weight. Similarly, when comparing the vehicle and buprenorphine groups, there is a main effect of time. There is also an interaction of drug (buprenorphine) by time in that vehicle-treated mice show a greater decline in weight than the buprenorphine-treated mice. In fact, the buprenorphine treated mice gain weight. When carprofen and buprenorphine-treated animals are compared, there is an interaction of time with treatment such that buprenorphine treated animals gain more weight than carprofen-treated animals. (**E**) Graph of % change in food disappearance from baseline. When comparing the vehicle vs carprofen group, there is a main effect of time such that there is a decline in food disappearance over time. We also see a time by

treatment interaction such that carprofen-treated animals do not decline in food disappearance as much as vehicle treated animals. When comparing the vehicle vs buprenorphine group, there is a main effect of time. In the buprenorphine treated group, there is a time by treatment interaction such that the buprenorphine-treated animals demonstrate the smallest decline in food disappearance. Finally, comparison of the carprofen and buprenorphine groups shows that there is an interaction between time and treatment such that buprenorphine-treated animals show the least reduction in food disappearance. (**F**) Tumor volume was monitored weekly for mice in all groups. There is a main effect of treatment such that mice treated with carprofen show a greater decline in tumor volume than buprenorphine-treated mice.

Significant effects of statistics in Supplementary Table S3.

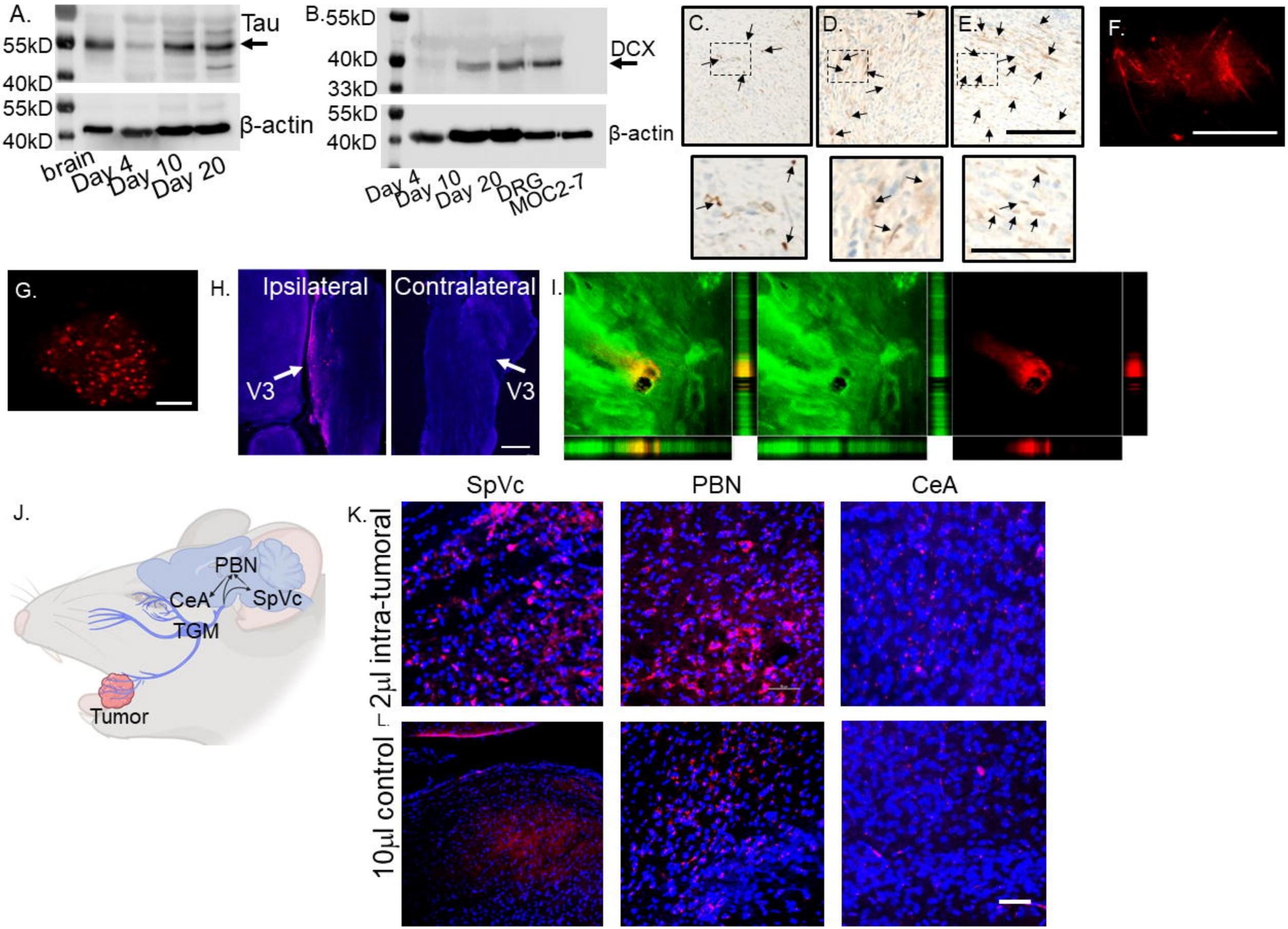
A.
55kD
40kD
Tau
55kD
40kD
β-actin
brain
Day 4
Day 10
Day 20
B.
55kD
40kD
33kD
DCX
55kD
40kD
β-actin
Day 4
Day 10
Day 20
DRG
MOC2-7
C.
D.
E.
F.
G.
H.
Ipsilateral
Contralateral
V3
V3
I.
J.
PBN
CeA
SpVc
TGM
Tumor
K.
SpVc
PBN
CeA
2μl intra-tumoral
10μl control

Figure 1

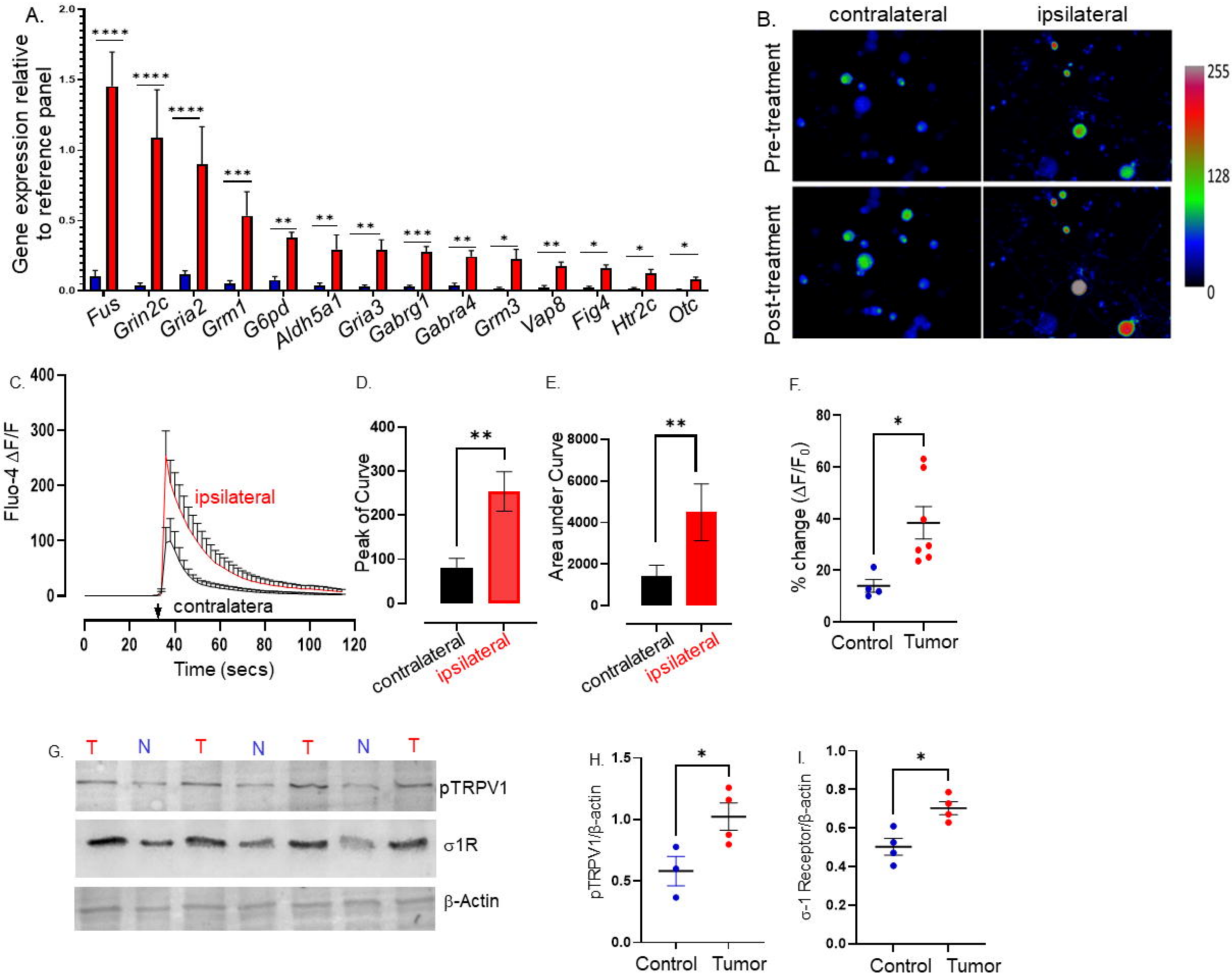
A.
Gene expression relative to reference panel
Fus
Grin2c
Gria2
Grm1
G6pd
Aldh5a1
Gria3
Gabrg1
Gabra4
Grm3
Vap8
Fig4
Htr2c
Otc
B.
contralateral
ipsilateral
Pre-treatment
Post-treatment
255
128
0
C.
Fluo-4 ΔF/F
ipsilateral
contralatera
Time (secs)
D.
Peak of Curve
contralateral
ipsilateral
E.
Area under Curve
contralateral
ipsilateral
F.
% change (ΔF/F0)
Control
Tumor
G.
T
N
T
N
T
N
T
pTRPV1
σ1R
β-Actin
H.
pTRPV1/β-actin
Control
Tumor
I.
σ-1 Receptor/β-actin
Control
Tumor

Figure 2

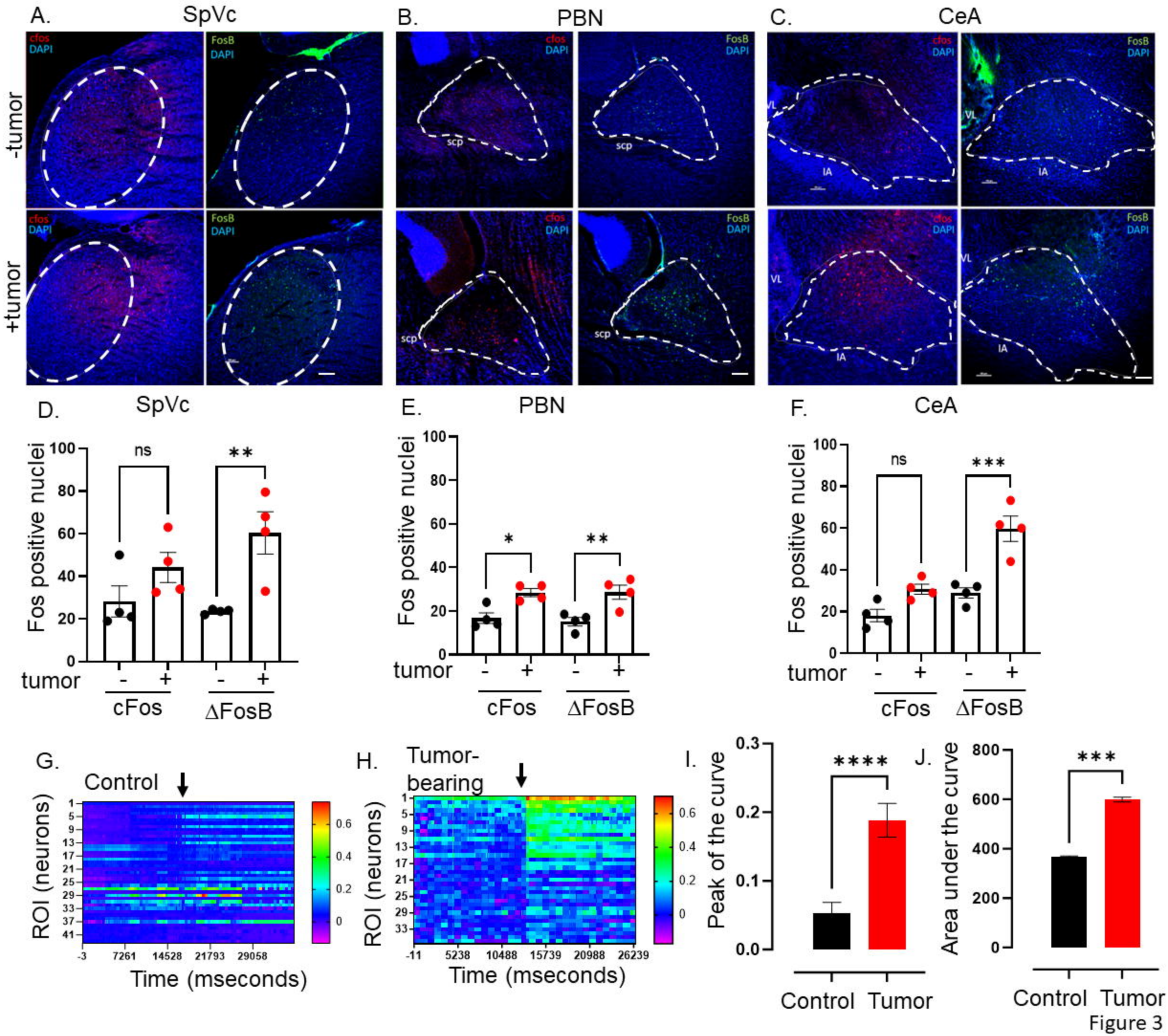
A.
SpVc
B.
PBN
C.
CeA
-tumor
+tumor
cfos
DAPI
FosB
DAPI
scp
VL
IA
D.
SpVc
E.
PBN
F.
CeA
Fos positive nuclei
tumor
cFos
ΔFosB
ns
**
*
***
G.
Control
H.
Tumor-bearing
ROI (neurons)
Time (mseconds)
I.
Peak of the curve
****
J.
Area under the curve
Control
Tumor

Figure 3

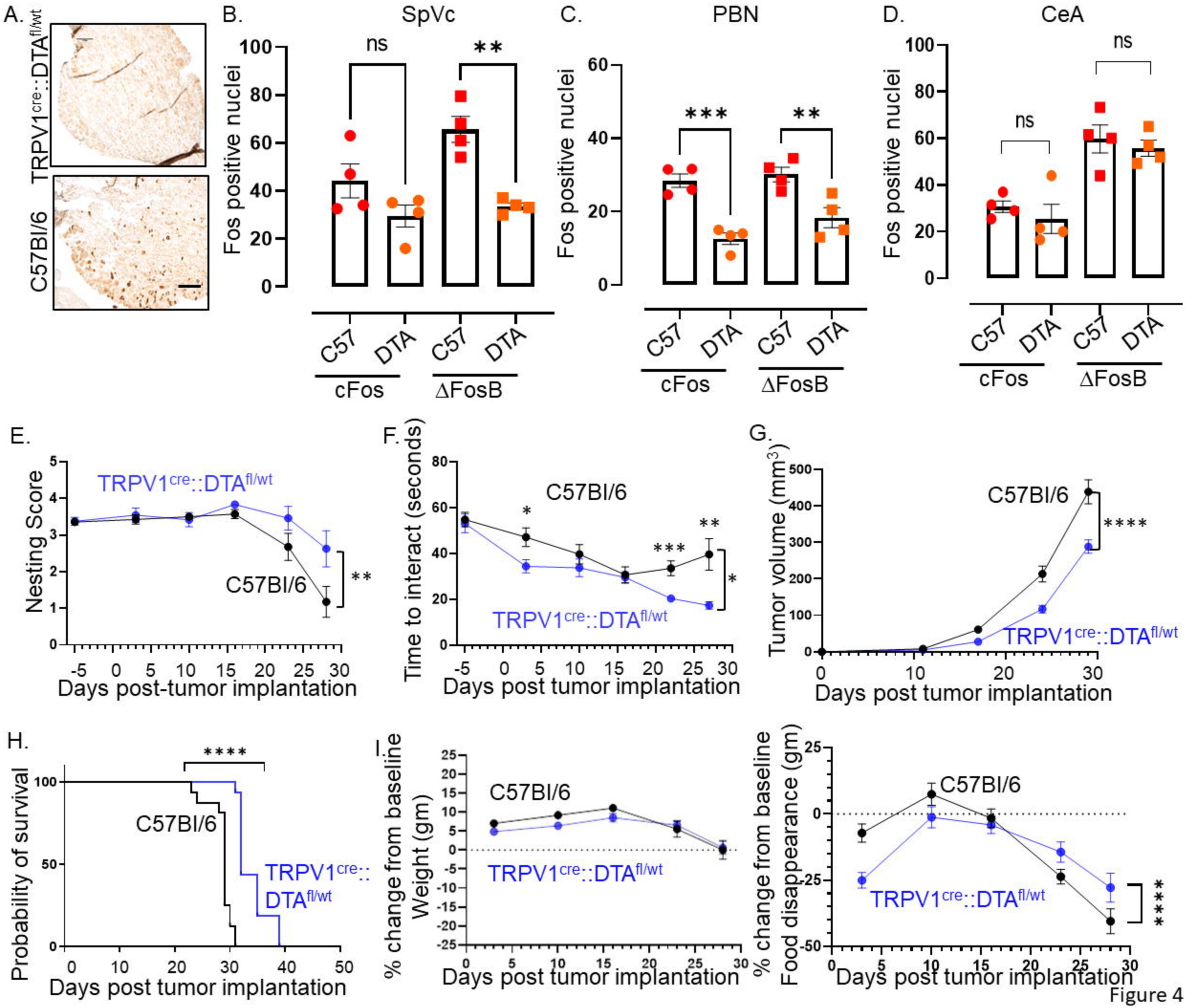
A.
TRPV1cre::DTAfl/wt
C57Bl/6
B.
SpVc
Fos positive nuclei
ns
**
C57
DTA
C57
DTA
cFos
ΔFosB
C.
PBN
Fos positive nuclei
***
**
C57
DTA
C57
DTA
cFos
ΔFosB
D.
CeA
Fos positive nuclei
ns
ns
C57
DTA
C57
DTA
cFos
ΔFosB
E.
Nesting Score
TRPV1cre::DTAfl/wt
C57Bl/6
**
Days post-tumor implantation
F.
Time to interact (seconds)
C57Bl/6
*
***
**
*
TRPV1cre::DTAfl/wt
Days post tumor implantation
G.
Tumor volume (mm3)
C57Bl/6
****
TRPV1cre::DTAfl/wt
Days post tumor implantation
H.
Probability of survival
****
C57Bl/6
TRPV1cre::
DTAfl/wt
Days post tumor implantation
I.
% change from baseline
Weight (gm)
C57Bl/6
TRPV1cre::DTAfl/wt
Days post tumor implantation
% change from baseline
Food disappearance (gm)
C57Bl/6
TRPV1cre::DTAfl/wt
****
Days post tumor implantation

Figure 4

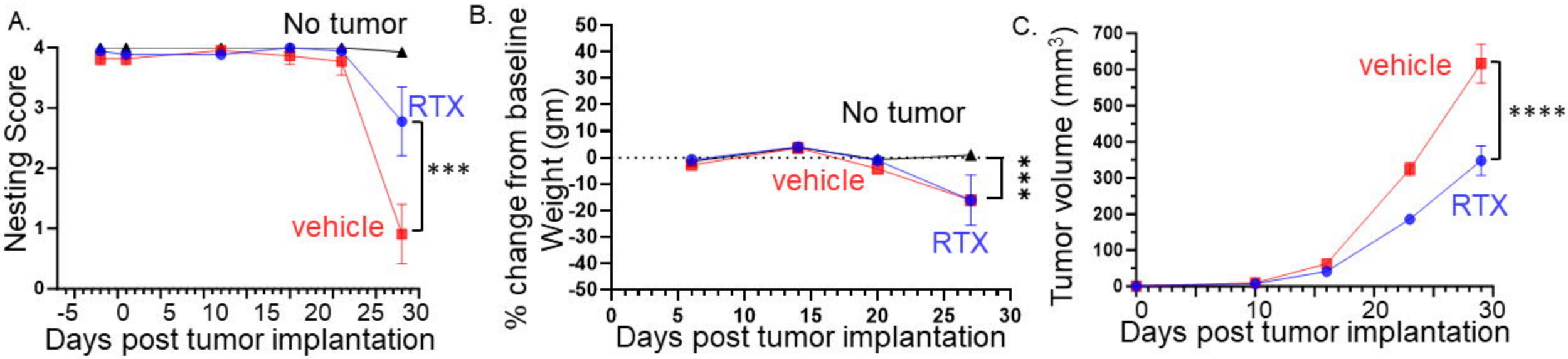
A.
No tumor
RTX
vehicle
***
Nesting Score
Days post tumor implantation
B.
No tumor
vehicle
RTX
***
% change from baseline
Weight (gm)
Days post tumor implantation
C.
vehicle
RTX
****
Tumor volume (mm3)
Days post tumor implantation

Figure 5

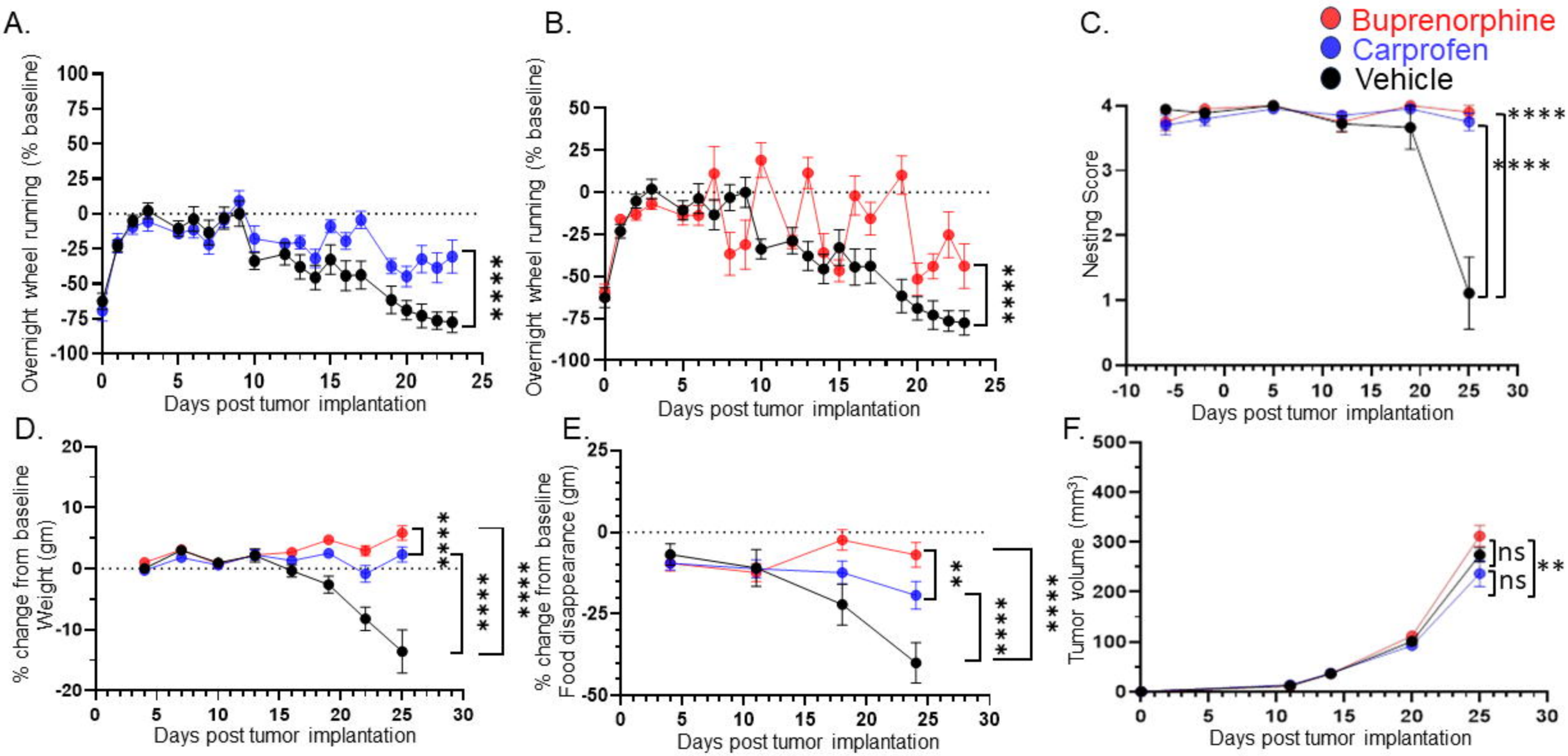
A.
B.
C.
Buprenorphine
Carprofen
Vehicle
Overnight wheel running (% baseline)
Nesting Score
Days post tumor implantation
D.
E.
F.
% change from baseline Weight (gm)
% change from baseline Food disappearance (gm)
Tumor volume (mm³)
ns
ns
**
****

Figure 6